1-10-2024

Ultrasonic phased array imaging and data post processing with applications to resistance spot welding

Milos Draskovic
University of Windsor

Ultrasonic phased array imaging and data post processing with applications to resistance spot welding

By

Milos Draskovic

A Thesis
Submitted to the Faculty of Graduate Studies
through the Department of Electrical and Computer Engineering
in Partial Fulfillment of the Requirements for
the Degree of Master of Applied Science
at the University of Windsor

Windsor, Ontario, Canada

2023

Ultrasonic phased array imaging and data post processing with applications to
resistance spot welding

by

Milos Draskovic

APPROVED BY:

_____

W. Kedzierski
Department of Physics

_____

B. Balasingam
Department of Electrical and Computer Engineering

_____

R. Maev, Advisor
Department of Electrical and Computer Engineering

December 19th , 2023

DECLARATION OF ORIGINALITY

I hereby certify that I am the sole author of this thesis and that no part of this thesis has been published or submitted for publication.

I certify that, to the best of my knowledge, my thesis does not infringe upon anyone's copyright nor violate any proprietary rights and that any ideas, techniques, quotations, or any other material from the work of other people included in my thesis, published or otherwise, are fully acknowledged in accordance with the standard referencing practices. Furthermore, to the extent that I have included copyrighted material that surpasses the bounds of fair dealing within the meaning of the Canada Copyright Act, I certify that I have obtained a written permission from the copyright owner(s) to include such material(s) in my thesis and have included copies of such copyright clearances to my appendix.

I declare that this is a true copy of my thesis, including any final revisions, as approved by my thesis committee and the Graduate Studies office, and that this thesis has not been submitted for a higher degree to any other University or Institution.

ABSTRACT

Resistance spot welding is a widely used metal joining method in the automotive industry due to its low cost, ease of automation and high throughput. Resistance spot welding is a process that joins two or more metal sheets through the application of force and high current in a localized region, or spot. With the average car containing thousands of such spot welds, some of which compose structural and safety components, the evaluation of the quality metrics related to this process is of key interest to the automotive sector. With this in mind, the evaluation of spot weld parameters including, size, penetration depth and yield strength have been evaluated using both destructive and non-destructive techniques. One of the more recent advancements involves the use of real time monitoring of the resistance spot weld using a single element transducer placed inside the welding electrode. This transducer allows for a determination of the penetration depth based on ultrasonic reflection at a single point within the weld stack. From this, other properties are estimated using the geometry and materials that are being welded. Such an approach works well in many cases but falls short as the industry shifts to ultra-high strength steels and aluminum materials, which are more prone to off-centre defects such as cracks and porosity. This work aims to overcome many of these challenges by replacing the current probe with a linear phased array version. Such a change allows for the monitoring of not only the weld penetration depth but also the lateral size of the weld alongside the detection of defects such as pores. This system would offer a significant advantage over current methods from a quality assessment standpoint. In order to realize these benefits, this work aims to bring such a system into a production-ready capacity. This includes designing a phased array system that is low cost and easy to maintain in a production environment. In addition to this, the methods of processing ultrasound data acquired with such a system require changes to existing methods, as the break in symmetry results in complications from an analysis standpoint. This work covers the methods and approaches used to reach these goals and bring the system closer to a production ready deployment.

ACKNOWLEDGEMENTS

TABLE OF CONTENTS

LIST OF TABLES

LIST OF FIGURES

LIST OF APPENDICES

CHAPTER 1
INTRODUCTION

1.1 Overview

Spot welding is one of the most common metal joining techniques used in the automotive industry. Through the proper combination of time, force and current, resistive heating within metal sheets can be used to weld these pieces together in a low-cost, rapid, and reliable manner.[1] However, with the adoption of new metals and alloys, and the resulting decrease in weldability, the likelihood of defects appearing during welding has increased. With the overall goal of increasing production output and minimizing defects, quality inspection methods for spot welds must also be improved, and new methods explored.

Quality inspection methods in the automotive industry typically fall into two categories. The first category is destructive testing (DT), which means that the integrity of the weld being inspected is destroyed and no longer functionable for its original intended purpose. The second category is non-destructive testing (NDT), which means that the integrity of the weld being inspected is kept and is still functionable for its intended purpose. The DT methods that will be employed here are known as the peel test and cross-sectional weld cut. The results obtained using these methods will be used as a comparison with the proposed method of NDT inspection that this research focuses on: Phased array ultrasound.

NDT can also be categorized further into off-line and in-line testing. Off-line testing is generally done after the weld is complete while in-line testing is done while the weld is being performed. In this work, the only offline method used will be that of ultrasound microscopy.

One of the currently employed techniques of in-line testing in the industry is the inspection of spot welds with a single-element ultrasonic transducer, which will be explored in chapter 4. This works by embedding the transducer into a spot welding electrode and monitoring the weld progress via ultrasound pulses in reflection mode. However, this method of inspection only monitors the weld along the center axis point,

and thus assumptions on the symmetry of the weld must be made. As the industry advances with the use of aluminum and high strength steels, these welds are more prone to off center voids which result in the single transducer method proving less effective.[1]

Technological advancements have allowed the possibility of using an ultrasonic phased array transducer, which is the focus of this work, to acquire the cross section of a weld being performed. This research focuses on the goal of optimizing geometrical lenses to increases the resolution of a linear phased array. By improving the quality of images produced, detection methods can be improved which will allow for a greater success in measuring the diameter of a nugget formed from a spot weld in real time. With the goal of bringing it to a state that's closer to commercial readiness and help improve reliability, cost effectiveness, and reassurance of the measurement device.

1.2 Thesis outline

The current chapter focuses on familiarizing the reader with common terminology, the problem at hand, and solution to be researched, as well as giving a brief outline of what is to be expected throughout the thesis.

Chapter 2 familiarizes the reader with the basic principles of the spot welding process, machinery, and equipment, as well as describing the destructive test methods in greater detail.

In chapter 3 the basics of ultrasound waves are discussed to familiarize the reader with the work conducted in this thesis. It also familiarizes the reader with non-destructive tests, how the data is processed, and the theory behind how transducers operate.

Chapter 4 discusses previous research, updates to the current research made, specifically the probe and acquisition system, and experimental setup.

Chapter 5 presents the data obtained, filters and algorithm used, along with the results of the post processing conducted to the data. Results are then compared and discussed.

Lastly, chapter 6 summarizes the results obtained, and future potential improvements are explored.

CHAPTER 2
THE SPOT WELDING PROCESS

2.1 Resistance spot welding process

The spot welding process involves two or more metal plates clamped together between two electrodes. A large clamping force is exerted typically in the 1000-2000 N range. Electric current is then allowed to pass through the sheets for a time. The time and current can vary depending on the metal being used, where steel is typically in the range of 5-12 kA is conducted through them over a period of 250-500 ms. Depending on the resistivity of the metal, the amount of current running through it, and the amount of time that the current is running, the heat generated (Q) in joules can be determined by Joule/Ohmic heating, governed by equation 2.1 shown below[2]:

$$Q = RtI^2 \qquad (2.1)$$

Where the electrical resistance, R, is measured in Ohms, time, t, in seconds and current, I, in amperes. This process is known as Joule Heating. Figure 2.1 can be shown depicting this spot welding process below:
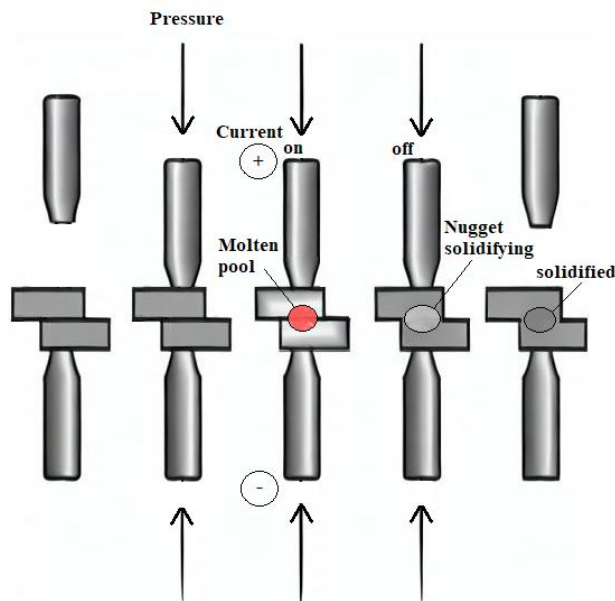
Figure 2-1 A depiction of the resistance spot weld process at various stages throughout a weld.

Through the proper application of current and time, the formation of a molten pool between the electrodes can occur, which upon solidification forms a solid bond. Industries typically have these parameters set prior to welding specific components. These pre-sets are referred to as welding schedules. For any given plate combination, there is often multiple combinations of current, time, and contact resistance caused by varying the clamping force that can be employed to form a satisfactory spot weld.[3] Note that in all instances an accumulation of heat may begin to occur if enough welds are performed. To ensure the electrodes don't overheat, cold water is constantly circulated through. This water-cooling system is also used to speed up the solidification of the nugget as it can help cool the plates down.

2.2 Equipment and machinery

Spot welding machines come in many different shapes and sizes. The ones that are present at the University of Windsor include both the X-gun arrangement and the C-gun arrangement. The spot welding machine associated with all the research done in this paper is the model TDC-5840 C-gun arrangement shown in figure 2.2 below. This arrangement was chosen because its movement only occurs in one dimension. This will limit error in alignment that a welding gun with multiple degrees of motion would encounter such as with the X-gun arrangement, where the jaws close in a scissor-like motion. These misalignments will be discussed more thoroughly in chapter 5.
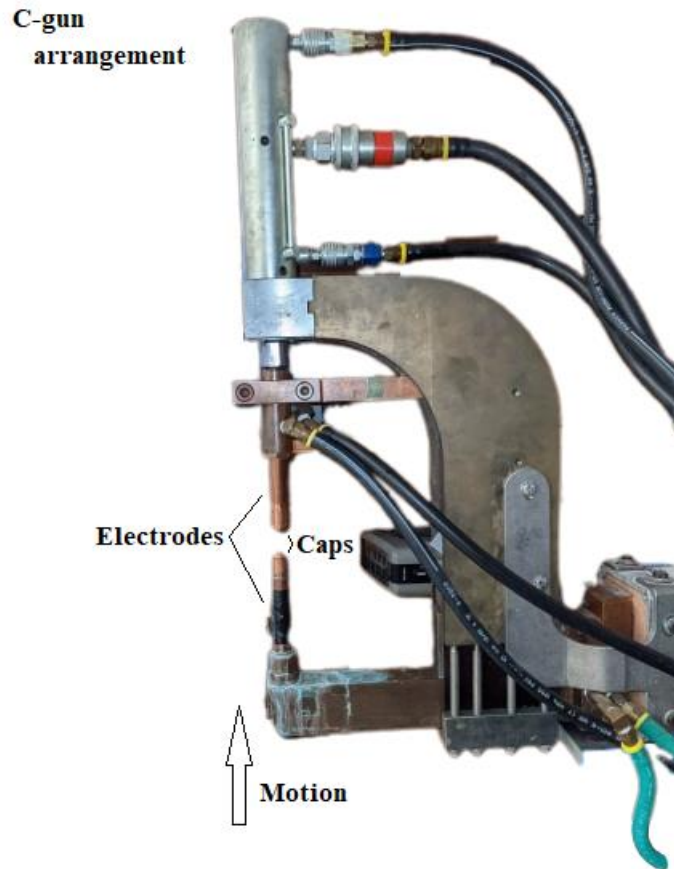
Figure 2-2 - C-gun arrangement used for the research conducted in this thesis. Located at the University of Windsor.

Additional important pieces of machinery that must be discussed are the electrodes and caps which can be seen in figure 2.3. Like the rest of the weld-gun, they are both typically made of copper or copper alloys. The reasoning behind this is due to their high thermal and electrical conductivity. With the caps serving as a way to focus current through the metal sheets, they experience rapid heating and cooling and thus must be able to dissipate this heat quickly to prevent welding itself onto the metal sheets.[4] Eventually they will wear down so they must be resurfaced and in turn replaced. Depending on the metal being clamped down, coating such as zinc which is often present on the steel to prevent rust formation can also melt and solidify on the caps, resulting in the formation of alloys that may further deteriorate the weld quality and wear to the electrode caps.

Figure 2-3 - A used cap with some degradation can be viewed on the left where the coating of the metal is observed to have solidified while an unused cap is presented on the right.

2.3 Destructive weld quality inspection methods

2.3.1 Peel test quality inspection method

The peel test simply involves pulling apart two metal plates so the size of the spot weld nugget holding them together is revealed. When the nugget is exposed a measurement of its diameter can be taken using a caliper. A couple of precautions must be taken when measuring the nugget using this method.

Metals that are malleable are prone to pieces of the metal remaining attached when pulled apart where the spot weld has occurred. These pieces of metal that remain attached to the spot weld result in a nugget that is more difficult to measure. They are often referred to as tongues and can be seen in figure 2.4 below. To allow for more accurate nugget measurements, careful metal sheet separation or pulling of the tongues off the spot welds are required. Although not done here, addition to the pull tests used here, additional equipment can be used to monitor the force under which a weld yields and the strain characteristics of the joint.

2.3.2 Cross sectional weld quality inspection method

The cross sectional quality inspection method is a multi step process that is typically only done in lab settings and during the establishment of welding schedules. It first starts off by picking a weld to be observed. The metal that the spot weld is located on is trimmed down to a smaller size so it can fit into a mould. A cross sectional cut is then made to the weld in the direction to be observed, often along the center of the weld. The piece of metal that contains the spot weld is then placed into a mold with the cross section exposed. A thermal epoxy is then used to fill the mould. After the epoxy solidifies only the cross section of the weld is exposed to be sanded down and polished to a mirror like consistency. By applying a Nital five per cent solution, or an alternative etchant based on the metals being used, the differing alloys within the weld are etched at differing rates, allowing for the metallurgical structure to be seen under a microscope. A common cross sectional weld image can be seen in figure 2.5 below along with the metallurgical structure that is to be observed.
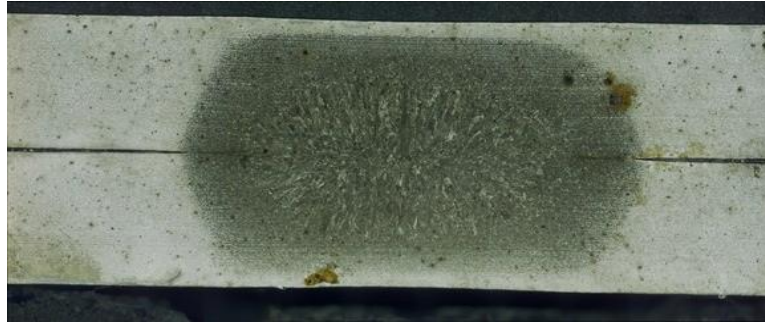
Figure 2-5 A weld cut cross section on the left imaged under an optical microscope where the regions of fused metal can be observed. On the right an image of where three cross sectional cuts are polished and await to be etched for observation.

CHAPTER 3

SOUND WAVES AND TRANSDUCER BASICS

3.1 Sound waves

Sound waves can be categorized depending on their frequency. The audible range for humans is known as the sonic range and operates at 20-20,000 Hz. Below and above the sonic range the wave propagating can be respectively referred to as infrasonic and ultrasonic respectively. The research proposed in this thesis dealt with sound waves emitted from a 15 MHz transducer and is therefore in the ultrasound regime. This region was chosen because it provides higher resolution images. The higher frequency sound waves can penetrate shallower depths but create detailed images of smaller structures. Lower frequency transducers, on the other hand, can penetrate deeper into the material but may not provide as much detail. The reasoning behind this effect stems from the fact that the speed at which a wave travels at in a medium can be approximated as a constant for similar frequencies. So, a higher frequency wave results in a shorter wavelength according to the wave speed equation provided below[5].

$$v = \lambda f \qquad (3.0)$$

Where v is the speed of sound in the medium, λ is the wavelength of the propagating wave, and f is the frequency of the wave.

Higher frequency sound waves have shorter wavelengths, allowing them to interact with smaller structures in a more detailed way. Depending on the material, different scattering regimes can be present when a wave encounters a boundary. If the wavelength is much shorter than geometric variations, specular reflections will occur, otherwise, diffuse reflections can result, which result in a notably lower reflection. This is why higher frequency transducers are often used to image smaller structures or regions of interest with greater detail.

The waves themselves can be further categorized depending on how they propagate through media. Since the region of imaging interest is within steel plates, a look at how waves propagate in solid materials must be observed. For solid materials, the sound can propagate via longitudinal waves, hear waves and more complex modes not

explored here. In figure 3.1 below, one can see the differences between shear and longitudinal modes. Although both waves are propagating in the same direction, the means of how they propagate vary. For longitudinal waves, the particles consist of regions of compressions and rarefactions, while shear waves have particles moving in the direction perpendicular to the wave's propagation direction through the bonds within a materials lattice. Shear waves propagate poorly in liquids or gases as their method of propagation relies on the strong bonds between particles.
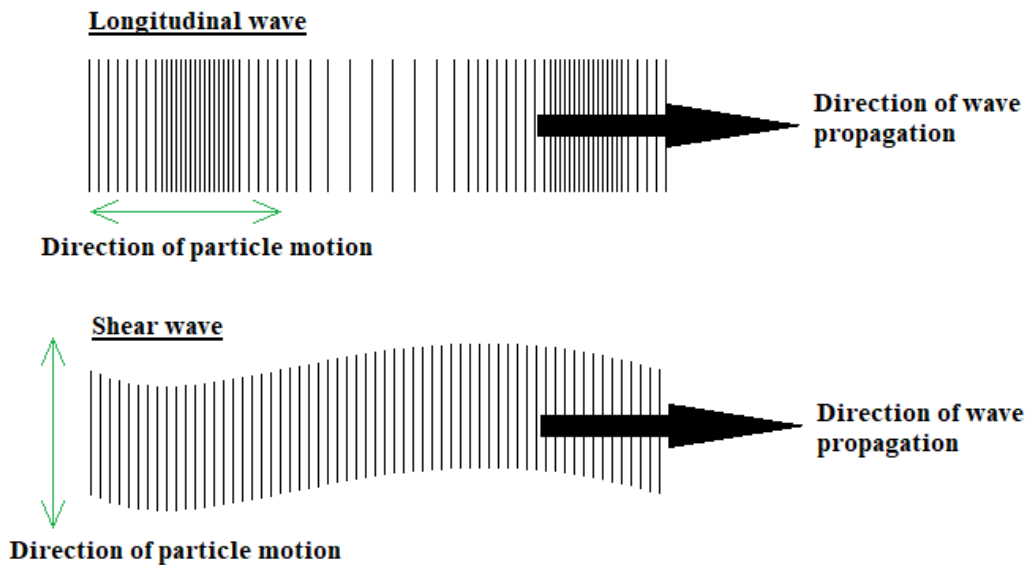
Figure 3-1 A longitudinal wave's particles move along the same direction as the propagating wave, creating regions of compression and rarefaction while the shear wave has particles moving perpendicular to its wave propagation direction. Note that shear waves are only present in solids as solids exhibit shear strength that hold the object in place.

Upon encountering a boundary between two materials, such as the liquid water to solid copper boundary, the longitudinal waves present can undergo mode conversion and continue its propagation as a shear wave through the solid.[5] Mode conversion is simply a term used to explain the phenomenon of a propagating wave's energy transforming into another form. Since the means of propagation for both types of waves vary, the speed at which they travel also vary. For reference, a 15 MHz frequency longitudinal wave in steel travels at a speed of approximately 6000 ms^{-1} while shear waves travel at a speed of approximately half that.[6] Shear waves in steel are seen to travel at a much slower speed than that of longitudinal waves, and because of the disparity between speeds, the waves

will refract at different angles. Even though this is the case, an effort is made to single out a mode of propagation to reduce artifacts that can result. In addition to the angle of transmission, the energy transmitted into a material is dependant on both the material properties, mainly the sound speed and density, as well as the transmitted angle. Figure 3.2 below shows the transmission coefficients of wave modes present upon a copper-water boundary as the incident angle changes.
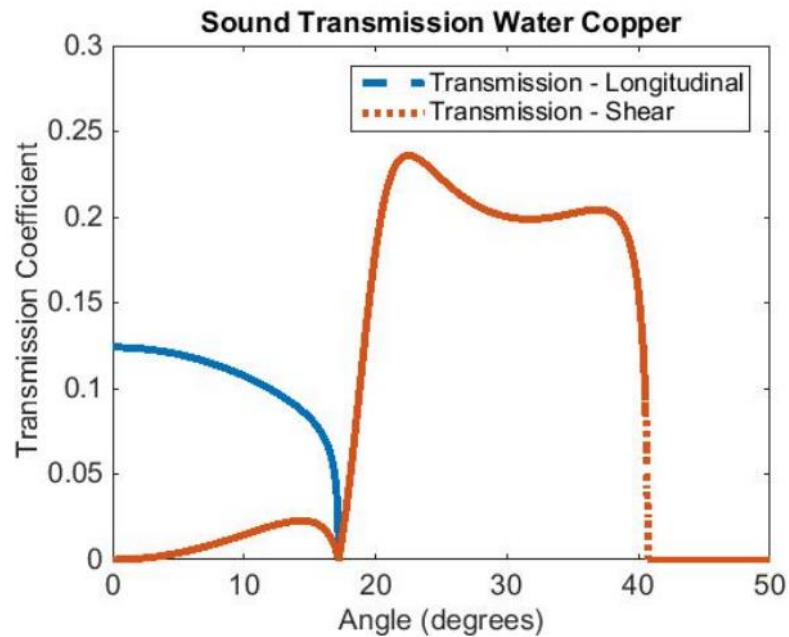
Figure 3-2 A plot of the transmission coefficients and mode conversion between the water-copper interface for shear and longitudinal waves. (Ouellette, 2015, Figure 2.3)[7]

Longitudinal waves are seen to be predominately present at low incident angles with respect to the normal. Although shear waves travel at slower speeds, meaning the reflections would not be seen within the selected time window, the research proposed in this thesis deals with angles below twenty degrees, so shear waves are rarely present.

3.1.1 Time of flight

Time of flight is the measurement of the time it requires for a wave to travel from a source to an object and back. It can be used to measure distances within media if the speed at which the wave is travelling in is known. A simple case where there is only one medium present can be modeled below by equation 3.1 where distance travelled in the

medium, d_m can be calculated by knowing the time, t_m, that the wave has travelled in the medium, and the speed of sound in the medium, v_m.[7]

$$d_m = \frac{(v_m * t_m)}{2} \qquad (3.1)$$

Note the factor ½ comes from the fact that feedback via pulse reflection mode requires the wa ve to travel a full distance of d twice on its way to and back from the point in question.

The speed of sound in the medium v_m can be calculated and will depend on the materialistic properties of the medium it is travelling in, where the speed in a solid state can be represented by equation 3.2 and the liquid state by equation 3.3 below.

The speed of sound in a solid depends on the elastic properties of the material, namely its Young's modulus (E), density (ρ), and Poisson's ratio (ν). The equation for the speed of sound in a solid is given by:

$$v = \sqrt{\left(\frac{E}{\rho(1-\nu)}\right)} \qquad (3.2)$$

Where v is the speed of sound in the solid, E is the Young's modulus of the solid, ρ is its density, and ν is its Poisson's ratio.

Young's modulus is a measure of the stiffness or elasticity of the solid, and describes the amount of force required to stretch or compress the solid by a given amount. A material with a higher Young's modulus is stiffer and has a higher speed of sound. Density is a measure of the amount of mass per unit volume of the material, and a higher density generally results in a lower speed of sound. Poisson's ratio is a measure of the material's lateral deformation in response to an applied longitudinal strain. It is the ratio of the transverse strain to the longitudinal strain and ranges between -1 and 0.5. Poisson's ratio affects the relationship between the longitudinal and transverse wave velocities, and therefore the speed of sound in the solid.

The speed of sound in a liquid depends on the compressibility (β) and density (ρ) of the liquid. The equation for the speed of sound in a liquid is given by:

$$v = \sqrt{\left(\frac{K}{\rho}\right)} \quad (3.3)$$

where v is the speed of sound in the liquid, ρ is its density, and K is the bulk modulus of the liquid.

The bulk modulus is a measure of the resistance of a liquid to compression and is related to the compressibility of the liquid. A material with a higher bulk modulus is more resistant to compression and has a higher speed of sound.

In general, the speed of sound in a liquid state is lower than in a solid state due to the weaker intermolecular forces that hold the liquid state together[8]. The speed of sound in these states can also be affected by the properties it is travelling in such as the temperature and pressure, with an increase in these two properties generally increasing the speed of sound in the media.

Once the speed of the sound in the media and the time of flight is known, if reflections are present, the distance from the transducer as well as the distances between reflectors can be calculated. This will be useful in determining the presence of a weld nugget in the ultrasound scans provided in chapter 5.

Equation 3.1 can be extended further to measure multiple distances along different media provided each of these waves are incident to the normal of boundaries present and reflections are observed. By measuring the time of flight between reflections, distances between these two reflectors can be obtained. When the waves incident upon boundaries are not at normal, refraction according to Snell's law will need to be implemented.

3.1.2 Snell's law

Snell's law for waves describes the relationship between the path taken by a wave in crossing a boundary between two contacting media with differing speeds. This law was founded back in 1621 by Willebrord Snellius and one of the ways it can be derived is by using Fermat's principle of least time. Fermat's principle for waves states that a wave travelling between two points will take the path that takes the least amount of time to travel. An arbitrary wave's path from point A to B can be represented by the pink line in figure 3.3 below and its time of flight can be represented by equation 3.4 below. By taking the derivative of this equation with respect to the position and setting it equal to zero, the positioning at which time of flight is minimized, and constructive interference maximized, can be found. By use of trigonometry, equation 3.5 results in equation 3.6 and is well known as Snell's law[9]:
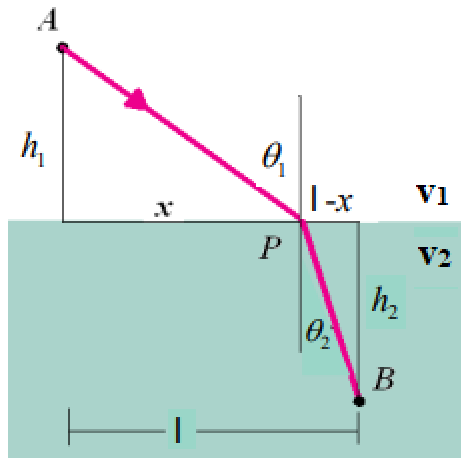
Figure 3-3 Arbitrary path from point A to B taken by a wave used to represent Fermat's principle of least time. (Haber, 2009, Figure 2)[21]

$$t = \frac{\sqrt{x^2+h_1^2}}{v_{l_1}} + \frac{\sqrt{(l-x)^2+h_2^2}}{v_{l_2}} \qquad (3.4)$$

$$0 = \frac{dt}{dx} = \frac{x}{v_{l_1}\sqrt{x^2+h_1^2}} - \frac{l-x}{v_{l_2}\sqrt{(l-x)^2+h_2^2}} \rightarrow \frac{x}{v_{l_1}\sqrt{x^2+h_1^2}} = \frac{l-x}{v_{l_2}\sqrt{(l-x)^2+h_2^2}} \qquad (3.5)$$

$$\frac{sin\theta_1}{v_{l_1}} = \frac{sin\theta_2}{v_{l_2}} \qquad (3.6)\ (Snell's\ law)$$

Where θ_1, and θ_2 respectively represent the incident and refracted angle of the wave with respect to the normal, and v_{l_1} and v_{l_2} represent the longitudinal speeds of the wave within the respective media found using equation 3.2 and 3.3.

By analyzing equation 3.6, it can be seen that the incident and refracted angle are proportional to one another. If the wave travels from a medium of slower speed into a medium of greater speed, then at a certain incident angle, the resulting refracted angle will be at a right-angle propagating along the boundary. The incident angle at which this occurs is known as the critical angle. Referring to figure 3.2, the relationship between wave modes and angles can be seen. Angles beyond the first critical angle of approximately 20 degrees result in only shear waves being transmitted while angles beyond a second critical angle of approximately 40 degrees result in sole reflection and surface waves if supported.

Note that even if the incident angle is below the critical angle, some of the wave will still be reflected. Using a similar approach, the angle at which a reflected wave propagates can also be calculated. An arbitrary path from point A to B can be seen to be represented by the pink line in figure 3.4 below. Note that the reflected wave stays within the same medium so equation 3.6 will simplify to equation 3.7 below, where the incident angle, θ_1, is equal to the reflected angle, θ_2.
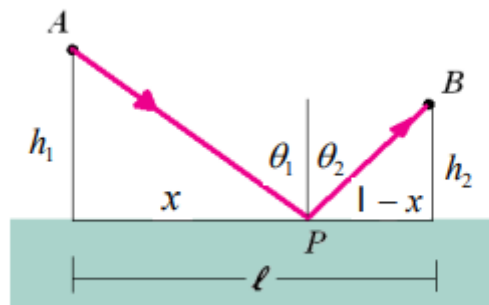
Figure 3-4 Arbitrary path from point A to B taken by a wave used to derive the angle at which waves reflect at. (Haber, 2009, Figure 1)[21]

$$\frac{sin\theta_1}{v_{l_1}} = \frac{sin\theta_2}{v_{l_1}} \rightarrow \theta_1 = \theta_2 \text{ (3.7)}$$

3.1.3 Impedance, transmission, and reflection

Through conservation of energy, energy cannot be created nor destroyed, thus for an incident wave to simultaneously reflect and transmit through a boundary's surface, it must split up its energy upon contact. To determine the intensity of the wave that gets transmitted and reflected, use of acoustical impedances is necessary. Acoustical impedance by definition is the resistance to the propagation of waves through materials and each material's impedance varies as represented by equation 3.7[8].

$$Z = \rho v \qquad \text{(3.7)}$$

Where impedance, Z is represented by the product of the medium's density, ρ with the speed of the wave within that medium, v. In the simplest case where a wave is incident normal upon a boundary, the reflection and transmission coefficients, R and T for pressure, p and intensity, i are seen in 3.8a-e below[10] .

$$T_i = \frac{Z_2}{Z_1}T_p^2 \qquad \text{(3.8a)}$$

$$R_i = R_p^2 \qquad \text{(3.8b)}$$

$$T_p = \frac{2Z_2}{Z_2+Z_1} \qquad \text{(3.8c)}$$

$$R_p = \frac{Z_2-Z_1}{Z_2+Z_1} \qquad \text{(3.8d)}$$

$$1 = T_p + R_p \qquad \text{(3.8e)}$$

In the case when an incident wave is not normal to the boundary, the equations are modified with respect to the angles observed using Snell's law such as in equation 3.9.

$$T = \frac{2Z_2 cos\theta_i}{Z_2 cos\theta_i + Z_1 cos\theta_t} \qquad \text{(3.9)}$$

In the work presented within the thesis, the transitioning of waves from liquid water to solid copper is important as any angle offset from the normal results in some mode conversion occurring. In this case, the use of equations below would be appropriate to find the intensity of transmission for longitudinal and shear waves[10]:

$$T_L = \frac{\rho_w}{\rho_c} \frac{2Z_L \cos(2\theta_S)}{Z_L \cos^2(2\theta_S) + Z_S \sin^2(2\theta_S) + Z_w} \quad (3.10a)$$

$$T_S = -\frac{\rho_w}{\rho_c} \frac{2Z_S \sin(2\theta_S)}{Z_L \cos^2(2\theta_S) + Z_S \sin^2(2\theta_S) + Z_w} \quad (3.10b)$$

Where,

$$Z_L = \frac{\rho_c v_L}{\cos\theta_L} \quad (3.10c)$$

$$Z_S = \frac{\rho_c v_S}{\cos\theta_S} \quad (3.10d)$$

$$Z_w = \frac{\rho_w v_w}{\cos\theta_i} \quad (3.10e)$$

$$R_p = 1 - T_L - T_S \quad (3.10f)$$

Where the subscripts w, and c, refer to the water and copper media respectively, and L, S, refer to the longitudinal and shear wave.

By analyzing the equations, it can be seen that at small angles the longitudinal transmission equation 3.10a is seen to resemble equation 3.8c, and the shear transmission equation 3.10b approaches zero, so in low incident angles the first set of equations 3.8a-3.8e hold as a good approximation to use.

The higher the impedance mismatch between the materials present in a boundary, the greater the intensity of the reflecting wave. To produce good results when imaging within the metals sheets all that is necessary is enough of the wave's energy to reach within the metal and an impedance mismatch to occur to produce a reflection to be monitored. The transitioning of the wave in an open-air setting into the metal would produce minimal transmission as the impedance mismatch is far too great. This can be seen when ultrasound scans are taken in hospital settings. The gel used acts as a couplet

to allow wave transmission from a transducer into the body. Coincidently, because of the nature of the setup with the resistance spot welding process, the water circulation present within the electrodes that are used to cool the metals, can also be used as a coupling material to allow sufficient wave transmission into the metals.

3.1.4 Attenuation

Impedance is not the only factor that affects wave propagation. Another factor that must be accounted for is attenuation. Acoustical attenuation is a measure of the energy loss of sound propagating through a medium. The two main sources of attenuation present come from scattering and absorption[10].

Scattering is a phenomenon that can occur when a wave interacts with the medium it is travelling through. For instance, as a wave travels through metal, the grains within the metal it interacts with can vary in size and orientation. Depending on these details, the wave can be influenced to reflect off in unpredictable ways. This also explains why higher frequencies are more readily attenuated than lower frequencies as their waves have shorter wavelengths and interact more readily with small particles and irregularities in the medium they are traveling through, leading to more scattering. A great analogy can be observed when looking at the sky. Since the light spectrum consists of a range of frequencies, when the higher frequency colors are more readily scattered in the smaller particles present in the air, it results in a blue color being observed.

The second source of attenuation is absorption which naturally occurs when some of the transmitted wave's energy travelling through the medium is converted into heat.

The attenuation of a wave's amplitude within a material at a given distance is commonly represented by equation 3.11 below, where A_0 is the wave's initial amplitude, α (cm^{-1}) is the attenuation coefficient and the distance propagated is x (cm).

$$A = A_0 e^{-\alpha x}, \; \alpha = \alpha_0 \omega^\eta \qquad (3.11)$$

Where the attenuation coefficient is expressed by the wave's operating frequency, ω, and a material dependent parameter, η. This material dependent parameter is typically a known value that has previously been measured by fitting experimental data. Analysis of

the equation shows that a greater attenuation results in scenarios where deeper propagation and higher frequencies are used, which is consistent with the two main sources of attenuation discussed earlier.

3.2 Transducer basics

Now that the basics of sound waves have been discussed, the next section of this chapter will be discussing transducers and how they transmit the information gathered from sound waves to a data acquisition system that can construct images. The Transducers associated with the work presented in this thesis rely on the utilization of piezoelectric elements to convert a mechanical force into an electrical signal and vice versa. The way this works is when a force is applied to a piezoelectric crystal and the crystal deforms, it results in a displacement of charge. This displacement creates a potential difference across the surfaces of the crystal where electrodes are typically attached, thus a mechanical force such as a sound wave can be converted to an electric signal. The process is also reversible which means when a potential difference is applied across the surfaces, the dimensions of the crystal will change accordingly. Depending on the direction of force applied on the crystal, the polarity of voltage induced will change. This entire principle is known as the piezoelectric effect and the relationship between the force and voltage induced can be derived as follows[11]:
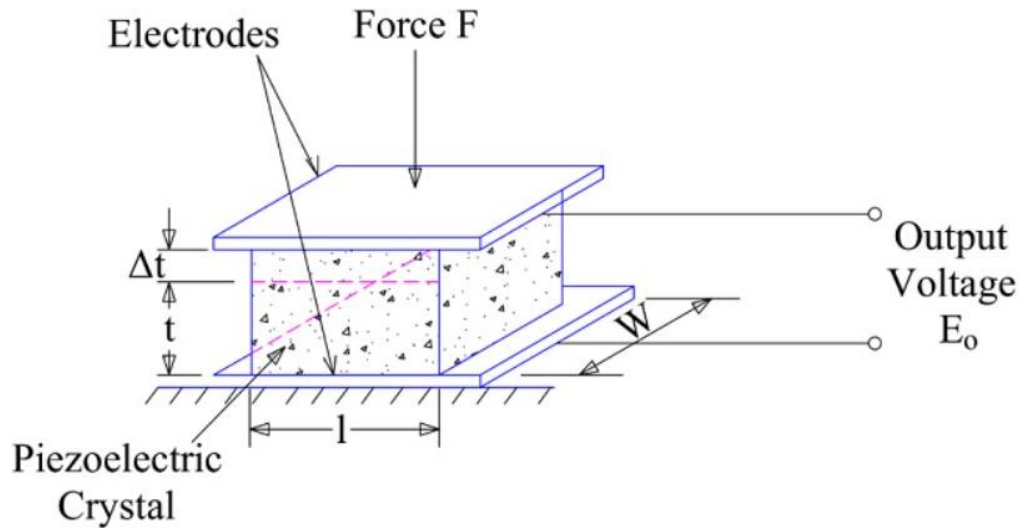
Figure 3-5 An illustration of a piezoelectric transducer displaying the piezoelectric effect. As a force is applied altering the size of the crystal, an output voltage is produced and vice-versa. (Electrical Baba, 2020, Figure 1).[22]

Starting with the piezoelectric equation, the relationship between the polarization, P, and stress, X, can be represented by (i):

$$P = kX \qquad \text{(i)}$$

Where k represents a piezoelectric coefficient. The polarization can also be represented by the charge per area (ii):

$$P = \frac{Q}{A} \qquad \text{(ii)}$$

While stress can be represented by the force per area (iii):

$$X = \frac{F}{A} \qquad \text{(iii)}$$

Substituting (ii) and (iii) into (i) results in (iv):

$$Q = kF \qquad \text{(iv)}$$

Which represents the relationship between force and charge. However, in sensor applications, the voltage is typically measured so the equation must be further derived. Using the electrostatic equation of a capacitor – represented by (v):

$$Q = CV \qquad \text{(v)}$$

Where Q represents the charge, C capacitance, and V voltage. Substituting (v) into (iv) and isolating for voltage results in (vi):

$$V = \frac{kF}{C} \qquad \text{(vi)}$$

Where the capacitance here is determined by the permittivity of the material under free stress, represented by (vii):

$$C = \frac{\varepsilon A}{t} \qquad \text{(vii)}$$

Substituting (vii) into (vi) results in equation 3.12:

$$V = \frac{kFt}{\varepsilon A} \qquad \text{(3.12)}$$

Observing the equation, it can be seen that the piezoelectric coefficient k, thickness t, dielectric permittivity ε, and area A are all constant for a given piezoelectric transducer. This means that the applied force is directly proportional to the output voltage across the electrodes.

Knowing how the transducer works to send and receive a signal, it's a matter of monitoring the reflections of a wave as it propagates through a medium to acquire the information necessary to construct an image. To understand how these images are constructed one must first start with understanding the A-scan.

3.2.1 A-scans

An A-scan is the most basic representation of waveform data consisting of a single pulse sent from a transducer through the material being tested[2]. The acquisition system essentially monitors the amplitude of the reflecting waves the transducer transmits over time and stores the data in an array where the time between each element is dependent on the acquisition rate of the transducer. If the speed of sound within the

media is also known, it will allow for the measurement of distance between reflectors. Figure 3.6 below shows the basic process of an A-scan acquisition.
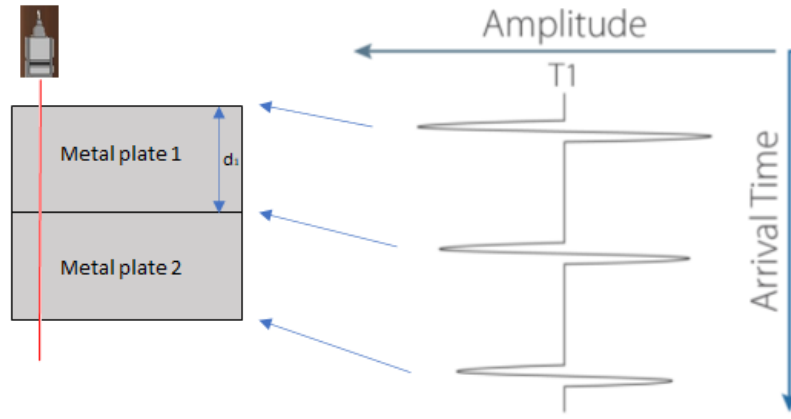
Figure 3-6 An example of a transducer sending a pulse through two metal plates where the reflectors observed arise from the boundaries and are presented by the amplitudes shown with respect to their arrival times. Note that the relative amplitude is determined by the magnitude and polarity of voltage measured.

Although the A-scan provides the necessary information to distinguish the distance between reflectors present in the wave's path, it does not contain enough information to yet construct an image. In order to do so, an additional dimension must be added. Depending on the approach, a B-scan or M-scan image can be observed.

3.2.2 B-scans

When multiple A-scans are taken along a dimension of space, they can be put together to form a 2-D array image with color-coded amplitudes. When these elements are displayed on a grey scale value, a brightness scan commonly referred to as a B-scan is acquired. Observing figure 3.7 below, it shows the A-scan which is the time of flight along one axis with transducer position along the other.
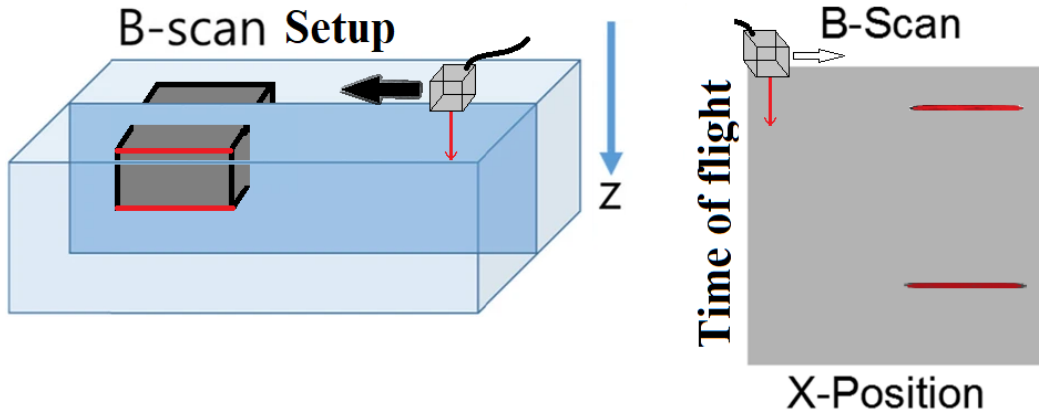
Figure 3-7 A B-scan setup on the left with a resulting B-scan image produced on the right. Note how the object appears larger in the B-scan image. This is due to the differing propagation speeds in differing media. In this example the waves travel significantly slower in the object, so the resulting image appears stretched out. Also note that the intensity of the color drops the deeper the wave propagates. (Adapted from Adelodun et al., 2020. Fig 3. Modified by author).[23]

The advantage to this method is it results in the ability to create a cross-sectional view as well as distinguish the position and size of reflectors present within the observed material. This method proves useful in scenarios where impedance mismatches are always present such as with visualizing layered materials such as laminates or coatings to help identify potential defects or disbanding between them. Although this method is not the case for spot welding because the metal is homogenous so the dominant impedance mismatch occurs when the state of the metal changes such as the nugget forming in the liquid state. Although the boundaries of the nugget can be seen in an A-scan, or B-scan, it is often the change in these images that gives us information of relevance to the weld process. For this reason, we often use the M-scan.

3.2.3 M-scans

The M-scan mode is used to record motion within the selected material. One of the ways that this can be done is by monitoring a stationary position over a span of time to observe any changes within the environment. In this work, an M-scan is used to observe whether a weld is developed at a targeted location. If multiple locations are observed to be welded, then the size of the nugget present can be approximately

measured to be within these bounds. A typical M-scan that is obtained can be seen in figure 3.8 below.
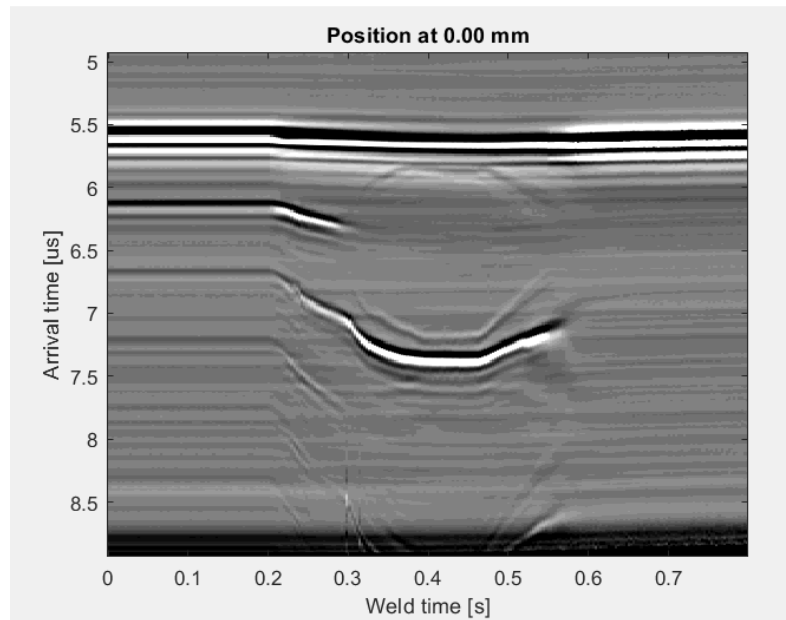
Figure 3-8 In this image a typical M-scan is observed at the center position of the array. Note how the image does not change for the first 0.2 s of the weld as nothing in the environment is changing. When the current is turned on the image starts to alter as the A-scans are encountering a change in environment. Liquid lines can be observed as the plate separation line begins to disappear at the 0.3 s mark.

Note that one axis represents the time of flight of the A-scan taken while the other axis now represents the time at which that specific A-scan was taken. By using this scanning method, the advantages that arise allow us to observe the exact time at which current turns on and off, if liquification occurs, and nugget penetration depth into the plates at that location. By observing multiple locations with this method, more information can be interpolated such as the shape and diameter of the nugget along the scanning axis. This scanning method, which will be discussed in chapter 4, allows for a characteristic signature to be acquired. To be able to scan multiple locations within a closed system such as inside an electrode an electronic phased array is the only suitable option as any mechanical movement, such as in raster scanning would be impractical to implement. For this reason, it was decided to explore the use of phased array ultrasound.

3.2.4 Phased array transducer

The phased array transducer consists of many small acoustical elements sending and receiving signals which work independently of one another.[12] To be able to

manipulate how each of these signals will interact with each other, a better understanding of Huygens's principle is necessary.

In 1678, a Dutch physicist known by the name of Christian Huygens derived a model used to describe various wave phenomena, from it arose Huygens's principle. This principle states that every point on a wavefront is itself a source of spherical wavelets, where each of these wavelets mutually interfere with one another.[13] The sum of these spherical wavelets results in the formation of a new wavefront. This effect can be seen in figure 3.9 below which shows when a wavefront is sent through a single slit experiment where the slit's size is equal to the wavelength of the wavefront. Upon reaching the slit, the entire wavefront is blocked off except at the location of the slit, where it is observed to emit spherical waves.

Incident plane wave   Wave past small opening
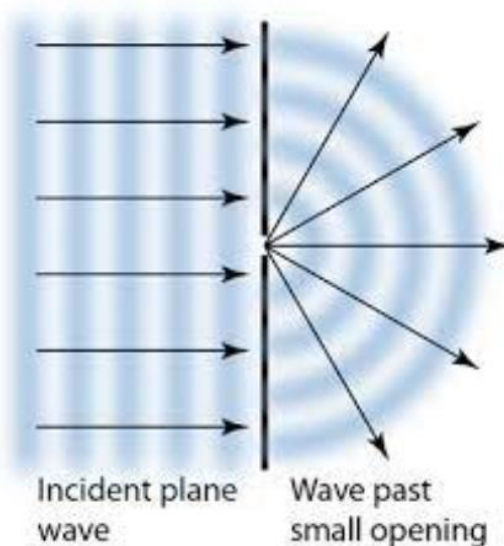
Figure 3-9 The Huygens-Fresnel principle states that "each point on a wavefront can be considered as a source of secondary waves" (Yu. H. 2020. Para. 2).[23]

This is important to know, because each element within the phased array is considered to act as a point source for waves to be emitted from. Thus, by controlling when these elements are fired off, the emitted wavelets can be constructively interfered with one another to steer and focus an acoustical beam on a particular position and depth.

Being able to steer and focus an acoustical beam using a phased array harbors many advantages when compared to its single element counterpart. Some of these include

reducing inspection time by cutting out the need for mechanical movement, as well as being able to change the shape and focal point of the beam as opposed to a single element transducer where these properties are fixed.

Although the beam and focal point of the array can be adjusted, there are still limitations within the beam itself which are dependent on the dimensions of the phased array's design. By modifying these parameters, one can optimize resolution to produce finer images for specified applications and avoid additional artifacts that may arise such as grating lobes. The specifications of the phased array used in our facility will be discussed more in Chapter 4. A phased array's dimensional parameters can be observed along with the results of changing each of them in figure 3.10 below.[14]
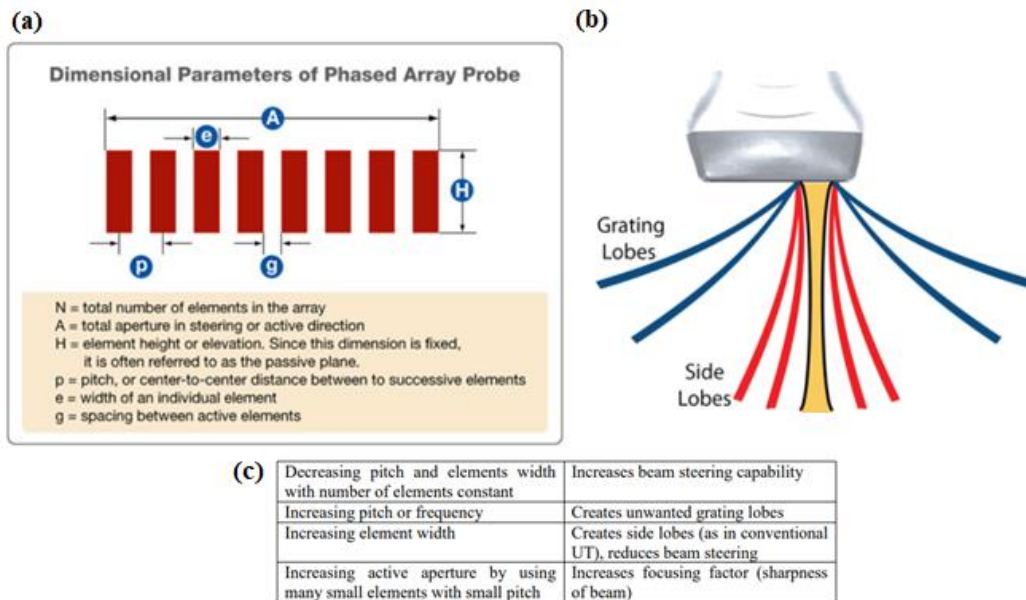
Figure 3-10 a) Standard dimensional parameters of a linear phased array probe (Olympus, n.d, Fig.1).[5] b) An image depicting one of many potential artifacts that a phased array probe may encounter. (Gupta et al., 2017, Fig. 6)[24]. c) A summary of some effects that are observed when the phased array parameters are altered.

Altering these parameters will influence the arrays effectiveness for the task presented. To summarize, in a linear phased array the total number of elements directly affects the directivity, sensitivity, and accuracy of beam steering, as well as the array's ability to suppress interfering signals from unwanted directions. However, increasing the number of elements may be limited by practical factors such as the size and spacing of the elements, and it also increases the overall complexity and cost of the system. The

total aperture or size of the array is also important, as it directly relates to the lateral resolution and directivity of the array, but larger apertures also increase complexity and cost. The pitch or spacing between elements affect the steering capability of the array and the depth focus of the beam but must be chosen carefully to avoid grating lobes. Grating lobes are spurious beams that occur when the spacing is not optimal. They will also occur if the individual elements are greater than or equal to the wavelength as the Nyquist limit is no longer satisfied. No grating lobes will be present if the elements size is less than one-half the wavelength, while elements of sizes between those two values will produce grating lobes depending on the steering angle. The width of individual elements affects the beamwidth and directivity. To improve the imaging resolution in spot welds, these parameters must be optimized.

Each of the parameters has an influence on the imaging ability of the system. For example, a larger total array size can in theory mean a better focal spot as the system is diffraction limited; however, if the array pitch is greater than half wavelength then there are likely to be artifact present as the Nyquist limit of sampling is not met. Generally, the choice of number of elements, size of the elements and the resulting total array size is a balance of imaging quality, cost, and practical limitations such as transducer assembly.

In addition to these concerns, the pitch of the array controls the inactive focusing ability. This portion acts as a single element transducer, meaning that we have no control over where this is focusing in a 1D array and it must be optimized to a specific depth of imaging.

3.2.5 Resolution

Resolution refers to the ability of the system to distinguish between closely spaced objects in the image being generated. There are several types of resolution that the reader should familiarize themselves with when optimizing a phased array ultrasound system.

Axial resolution refers to the ability of the system to distinguish between objects that are separated in the direction of the ultrasound beam. It is primarily determined by the spatial pulse length (SPL) of the ultrasound wave. SPL is the number of cycles

between the emitted ultrasound pulse as measured at full width half max. Typically, the shorter the pulse length, the higher the frequency of the wave. The formula for calculating axial resolution can be seen in equation 3.13 below.[15]

$$Axial\ resolution = \frac{1}{2}\ SPL \quad (3.13)$$

Where,

$$SPL = number\ of\ cylces\ in\ pulse * \lambda$$

Note that the wavelength is dependant on the medium it is travelling through and thus the axial resolution for a certain frequency will vary depending on the media the wave is propagating through.

Lateral resolution refers to the ability of the system to distinguish between objects that are close together in the transverse plane (perpendicular to the direction of the ultrasound beam). This is primarily determined by the width of the ultrasound beam and the focusing capabilities of the array. The lateral resolution can be calculated using equation 3.14 below.[15]

$$Lateral\ resolution \cong beam\ width = \frac{\lambda f}{D} \quad (3.14)$$

Where λ represents the wavelength of the wave in the medium, f represents the focal length (not to be confused with frequency), and D represents the aperture width of the array.

Contrast resolution refers to the ability of the system to distinguish between different material types based on their acoustic properties. It is determined by several factors, including the amplitude and frequency of the ultrasound signal, the quality of the electronic components in the system, and the quality of the signal processing algorithms used to reconstruct the image.

Temporal resolution in ultrasound imaging encompasses two key factors. Firstly, it relates to the system's ability to capture rapid changes and movements in the imaged material. This aspect is primarily determined by the frame rate, which represents how

many images the system can acquire and display per second. A higher frame rate results in better temporal resolution as it allows for the real-time visualization of fast changes. Secondly, temporal resolution is influenced by pulse duration, which impacts the precision of timing for returning echoes. Shorter pulse durations enhance temporal resolution by enabling the system to distinguish echoes from different depths with greater accuracy.

Lastly, selecting the depth of field in a linear phased array is also important to optimize imaging resolution. Depth of field refers to the range of depths over which the system can maintain good image quality. Depth of field is influenced by the size and shape of the ultrasound beam, as well as the focusing capabilities of the transducer. It can be calculated by utilizing equation 3.15 below.

$$Depth\ of\ field = 2\left(Near\ field\ length + \frac{Axial\ resolution}{2}\right) \qquad (3.15)$$

where the near field length which is commonly known as the near zone or Fresnel zone, is the region close to the transducer where the ultrasound beam is still converging and the beam diameter is changing rapidly. The near field length can be found via equation 3.16.

$$Near\ field\ length = \frac{D^2}{4\lambda} \qquad (3.16)$$

Where D represents the aperture of the array and λ represents the wavelength.[15]

3.2.6 Delay laws

A delay law, which is the time it requires for the next element within the array to be fired off so its wavelet can reach a target location at the same time as the previous element, can be calculated if the spacing between elements, distance between the center of each element to the refracting interface, and coordinates of the target focal point are known.[12]
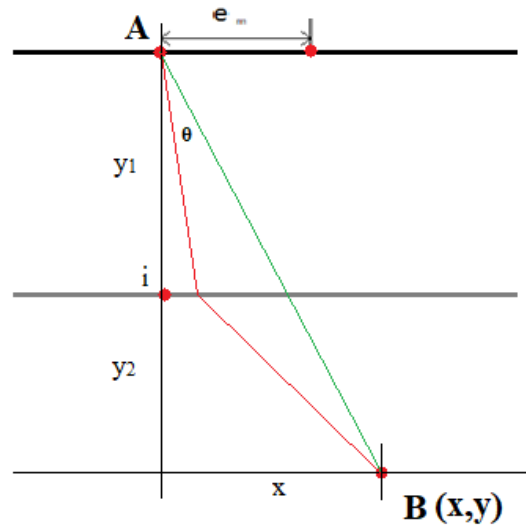
One of the ways the time delay for the center element A to target position B can be obtained is by a brute force method using Fermat's principle of least time. This approach starts off with calculating the time of flight of the direct path from point A to B which is represented by the green line and comparing it with a new path taken that has a small deviation from the direct path such as the red line in figure 3.11. If the new path has a time of flight that is shorter than that of the direct path, then the new path is the better choice. For any given set of paths, the region of maximum constructive interference will occur as the time difference between paths is zero. As this will typically be at a turning point, the minimum time will be the optimal path.

When the time of flight for an element is minimized, the same approach for the next element's path which is a known pitch distance of e_m away from the previous element. This process is then repeated for each element in the array. By taking the difference between the path with the minimized time of flight, a time delay is obtained, where the element with the greatest time-of-flight will be fired off first with subsequent elements firing off at times equivalent to these calculated time delays so that all the waves arrive simultaneously and constructively interfere at the target point B.

This code had been previously written by a student within the research group where appropriate adjustments were made to match the changes in the environment presented.[7]

CHAPTER 4
EXPERIMENTAL SETUP AND DESIGN

Current industry settings make use of a variety of inspection methods as previously outlined. One such system is the real time inline spot weld analyzer (RIWA). This technology was developed within the IDIR research group at the University of Windsor. It was implemented as a solution to the problems that offline testing methods encountered in industry settings.[16] Although offline testing methods result in a greater quality analysis of the weld, must be performed by trained employees and thus require more resources to do so. As the automotive industries alone performs thousands of welds on a single car, and thousands of cars built at a single plant per day, the ability to monitor each weld via offline methods is impractical. This time constraint leads to a selective process being used which may result in undetected problems occurring. When such selective inspection finds flaws, additional testing must be done to find a repair any vehicles prior to the last known good sample.

With the implementation of the RIWA, a single element transducer is embedded into the water cooling of the electrode to monitor the spot weld process along a single axis in real time. As heat and state changes occur within the metal being observed as it melts, additional boundaries are created between these states and can be seen within the ultrasonic A-scan data collected due to impedance mismatches. The A-scan data taken over time can then be put together in a 2D image with color-coded amplitudes to form an M-scan image, where an inference can be made on the state of the weld. An M-scan with highlighted signature features can be seen in figure 4.1 below.

Current on   off

1) Copper-steel reflection front plate
2) Reflection between steel plates
3) Copper-steel reflection back plate
4) Top of liquid steel pool
5) Bottom of liquid steel pool
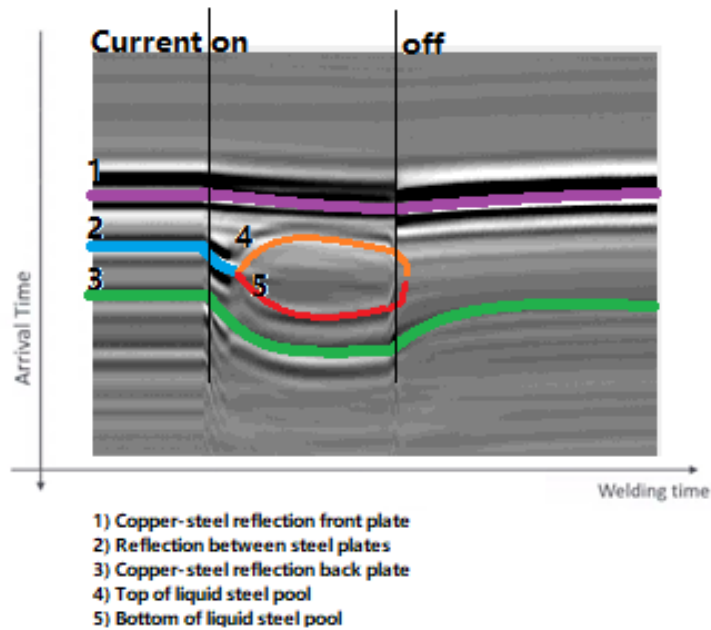
Figure 4-1 An ideal M-scan with signature features labelled to be detected

Although this method of inspection is a solution to the problems that offline inspection methods encountered; it is still limited in the sense that only the center axis of the weld is monitored. Due to its limited field of view, undetected problems can arise that ruin the integrity of the weld such as voids present off center and misalignment issues which may result in a misinterpretation of the weld.[7] In instances where a weld is considered a critical one such as those involving vehicle seat belts, sole reliance on RIWA's inspection is insufficient, thus the use of a linear phased array was explored.

4.1 Previous work

Two instances of research were previously conducted using the phased array within the IDIR research group where the optimization of the array was desired.[17,7] The work initially began with implementing the system in a spot weld machine as a prototype design. As the initial prototype lacked optimal imaging along with other problems, further research was conducted where a complete redesign of the system was explored to improve image quality and design implementation. This chapter will briefly cover the previous systems as well as the updates made to the latest system along with the experimental setup. A comparison of each design's specifications can be observed in table 4.1.

4.1.1 Prototype design

In the prototype design, it consisted of a 10 MHz phased array probe embedded in a larger copper housing that was mounted onto the shank of the electrode. The housing was drilled with an inlet and outlet at the sides to provide water cooling within the system via tubes. This design was manufactured by Centerline Limited, and an image of this prototype's final design and device can be seen in figure 4.2 below.
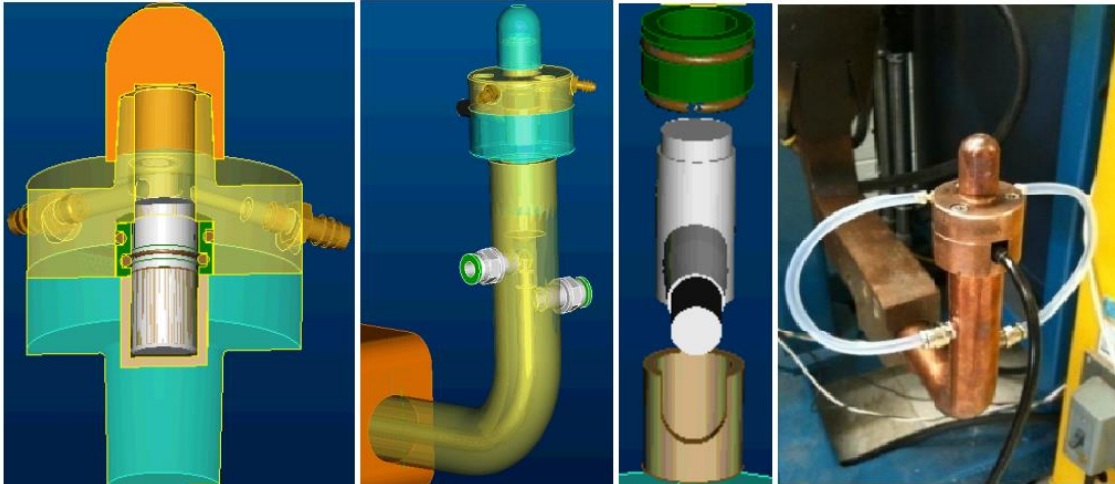
Figure 4-2 The prototype design can be seen on the left while the image on the right shows the final assembly. (Lui, 2012, Fig. 3.4.2 and 3.4.4)[17]

A larger housing was necessary at the time as the array's dimensions were not optimized for placement within a standard electrode shank. This housing design also created several problems on the quality of images produced. One of the major problems that occurred was air bubbles accumulated within the electrode due to the placement of the inlet and outlet holes. These bubbles affected the signal strength as air's high impedance greatly impacted the transmission of the waves and were difficult to eliminate making it impractical in an industry setting. Another major problem was the aperture of the probe was too small. Since phased array focusing relies on delay laws, a proper aperture must be selected to allow for the necessary focusing. It was found that a proper focus could not be achieved with this setup and thus a redesign was implemented.

4.1.2 Previous array

The second piece of work conducted in our group started with a simulation of tests using a 2D acoustic model to evaluate the old design. These tests consisted of

monitoring the intensity of the wave within the region of interest in both the elevation and phased direction. In the elevation direction, the spatial spread was found to have a full width half max (FWHM) of 2.6 mm, which indicated that any image obtained would be an averaging of features over this range. In the phased direction the probe was found to have a FWHM of 1.80 mm which indicated that no object smaller than this size could be discerned. Taking these results in mind, a redesign of the system with the goal of optimizing imaging was explored.

With the redesign of the system, it allowed for the ability to house the phased array into existing equipment using a 1-inch copper shank seen in figure 4.3. This was later reduced to ¾ inch, which allows for integration into an existing shank used in factories. The shape of the array was selected to be rectangular as fitting it into the cylindrical shaped electrode shank allowed water to still flow through the gaps present in each side. Since the array had already been assembled, there was no way to insert it without modifying the current electrode into multiple parts. An image of the transducer housing and assembly can be seen below in figure 4.3.
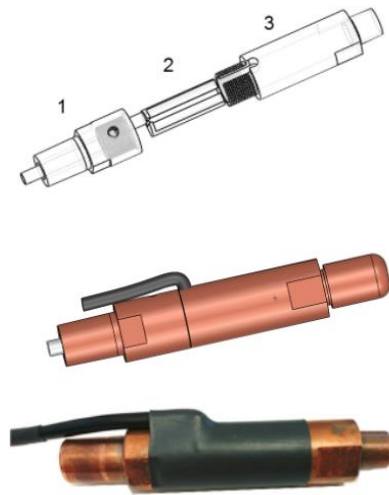
Figure 4-3 The image depicts the internal housing (2) and external housing (1&3) design of the transducer with the finished product at the bottom. (Ouellette, 2015, Fig. 3.12)[7]

Through a series of tests that had been previously conducted, the array's, parameters were optimized where the beam resulted in a FWHM of 0.9 mm. Since then,

the latest array has had some improvements. A direct comparison of the specifications of the two arrays can be seen in table 4.1 below.

Specifications	Previous Array	Newest array
Frequency	10 MHz	15 MHz
Number of Elements	16	24
Element Size	0.45 mm	0.45 mm
Inter Element Spacing	0.05 mm	0.05 mm
Elevation	5 mm	5 mm
Pitch	0.5 mm	0.34 mm
Aperture	8.00 mm	8.16 mm
Pulse Duration	≤ 250 ns	≤ 250 ns
Bandwidth	65 %	65 %

Table 4-1 Displaying the similarities and differences between the previous array and newest array.

With an increase in the frequency, direct improvement on the axial resolution occurs. A largest element count is necessary as the array elements are smaller in size. This provides greater beam shaping to achieve a higher lateral resolution, and a slight increase in the aperture leads to an increase in the depth of field. The dramatic decrease in pitch can help improve lateral resolution by allowing the array to sample the acoustic field more finely as well as increase the beam steering capabilities.

In addition to the improvements made on the resolution capabilities, the housing of the newest array had also been altered. Since the newest array's element contact points had not been soldered yet, the array's cable was able to be fed through a drilled hole made in the electrode where an epoxy was used as a seal to prevent any water leakage. This resulted in a single electrode piece being used as opposed to the previously modified one which consisted of three parts. To ensure that the probe doesn't shift from its initial position, an internal cylindrical housing was 3D printed to allow a snug fit. An image of the outer and inner housing can be seen in figure 4.4 below.

Figure 4-4 On the left the latest external housing of the array which consists of a single electrode piece with a hole drilled on the side to allow the array cable to be fed through. This method minimizes potential problems such as leakages which the previous multi-part housing consisted of. On the right the internal housing can be seen which consists of two cylindrical hollow tubes which allow adequate water flow while stabilizing the array in place.

4.3 Data acquisition system

In the two previous instances of research, the acquisition system that was used to store the data transmitted from the phased array was the Ultrasonic Open Platform[18] (Ula-OP) phased array system. At the time, it consists of up to 64 independent channels and 192 elements through a 1-3 multiplexer arrangement with a 12 bit receiver resolution system, maximum sampling frequency of 50MHz and pulse repetition frequency (PRF) of 25kHz. The bandwidth of the system ranged from 1-16 MHz. As this system was built for the medical field and for lab use, it was not suitable for use outside of initial prototyping.

The Advanced OEM Solutions (AOS)[19] is also an open platform data acquisition system controlled via software API. The specific model used for the research conducted in this thesis was the OEM-PA Miniature instrument where its specifications consist of up to 64 independent channels multiplexed with a receiver resolution of 14 bits, maximum sampling frequency of 100 MHz and PRF of 20kHz where higher options are available. The bandwidth of this system ranged from 50 kHz to 20 MHz. With an increase in sampling frequency, bandwidth range, and receiver resolution, the AOS system is a better fit for the application of inspecting resistance spot welds as AOS has a higher receiver resolution and gain range compared to Ula-OP, which allows for better

signal-to-noise ratio and image quality. Secondly, AOS has a wider bandwidth range of 50 kHz to 20 MHz compared to Ula-OP's 1-16 MHz bandwidth range, which allows for higher frequency probes to be used and potentially higher resolution images. Additionally, AOS has a smaller form factor, low power consumption, and high data transfer rate, making it more convenient and efficient for field inspections. Finally, as AOS comes in multiple channel counts, it can be deployed specifically to any final probe design, with the choice of 64 elements chosen for it's use in other projects within our research group. An image of this AOS board can be seen in figure 4.5.

Figure 4-5 An image of the AOS acquisition system board.[19]

4.4 Experimental setup

In this work, hundreds of welds were conducted and monitored under different parameters where thousands of ultrasonic scans were acquired and observed. With the goal of measuring weld nugget diameters using the phased array, the experiment was conducted in a manner where varying size nuggets were aimed to be created to replicate an industry like environment. The nugget sizes were attempted to consist of varying sizes of 2 mm, 4 mm, and 6 mm welds where ten of each size were aimed to be created. In addition to different nugget sizes, varying plate thicknesses and combinations were selected. The two plate thicknesses used were thin (0.70 mm) and thick (1.60 mm) plates which result in four different possible permutations. In this case, the order of plate placement is important as the array scans from a single side, so it's important to observe both thin-thick and thick-thin plate weld stacks as one may result in an improved image

quality and processing over the other. Orientation of the plates is also important as the array takes a single cross section across the nugget in a sweep, so comparing results to other methods such as the Scanning acoustic microscope (SAM), peel test, and cross sectional weld cuts, the orientation must be preserved. With three different nugget sizes and 4 different plate permutations, the geometry of the electrode caps used were also altered. The cap's geometry act as a method to focus the beam of the array. The geometries implemented were the flat, spherical, and cylindrical cap. An image of these caps can be seen in figure 4.6 below.

Figure 4-6 An image of a flat, spherical, and cylindrical cap is respectively shown above. Note that the flat cap's interface was polished.

While repeating the experiment under the three different cap geometries and keeping the other parameters consistent, a total of 360 welds were performed with each weld producing 7 different temporal scan positions by the acquisition system, a total of over 2500 scans were observed.

Since the cross sectional weld cut is a costly, lengthy, destructive process, only 25 cuts were conducted and observed. The rest of the welds were peel tested with select welds also being scanned by the acoustic microscope. Comparisons between the results obtained from the phased array, acoustic microscope, cross sectional weld cuts, and peels can be found in chapter 5.

CHAPTER 5

DATA ACQUISITION & IMAGING METHODS

5.1 Phased array data collection

To collect the data with the phased array, the welding machine pedal, which produces a 120 V signal to inform the welding gun to commence the weld, was also connected to an Arduino board through a voltage transformer. When the Arduino board received this signal, the AOS system connected to MATLAB commenced the acquisition process using a pre-programmed sequence. With every weld performed, the force, current, cap spot size diameter, plate orientation, and welding time were also recorded for replication of the experiment with differing cap geometries.

With every cap copper thickness varying, the distance from the transducer to the water-copper interface will also slightly vary. It is important to acquire this distance whenever a cap is replaced for image focusing calibration purposes. One must also remember to make sure that the distance is calculated after a weld has been performed because the massive amount of force that is used in a weld can displace a newly placed cap and significantly alter the distance from the array. To accurately obtain this distance, the entire system can be set to have the speed of sound equivalent to that of water because water is the only medium that is present up until the cap's copper interface. When the system is set this way, an A-scan occurring at the center of the weld can be viewed where the first major reflection represents the first interface (water-copper), and its time can be recorded. The distance between the array and copper interface can then be calculated.
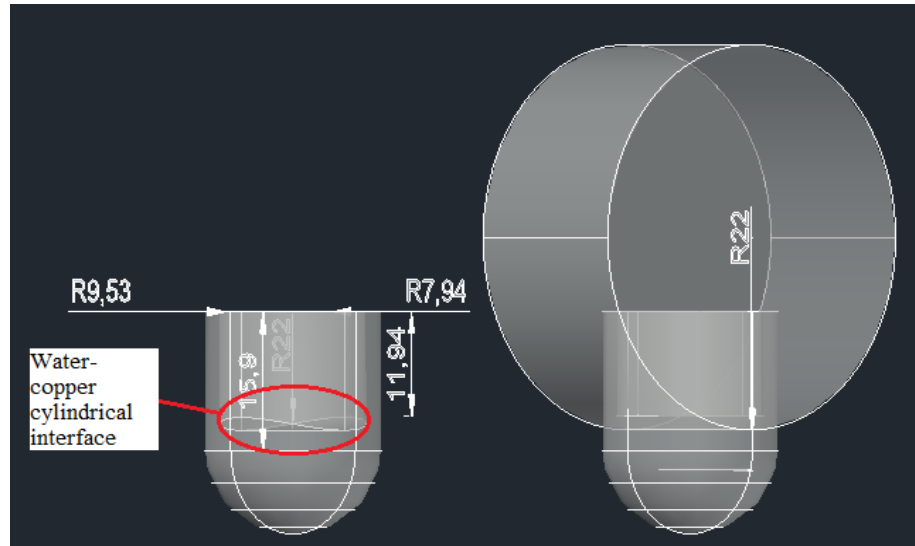
Depending on the cap's geometry, the distance from the array to the copper interface can also vary depending on the position along the scanning axis. For the flat cap the distance is constant throughout the whole scanning axis and can be obtained using the method mentioned in the previous paragraph. For the cylindrical cap the distance from the array is also constant throughout the scanning axis provided that the cap is oriented such that the cylindrical axis is parallel to the scanning axis. This can be observed in figure 5.1 above. For the spherical cap the boundary of the cap across the scanning axis will vary according to the equation of a circle as shown below:

$$(r)^2 = (x)^2 + (z - z_0)^2 \quad (5.1)$$

Where the parameter r is the radius of the circle previously selected within the IDIR group for optimised image focusing for a single element transducer with a set value of 22 mm. x is the distance along the scanning axis with respect to the center, z-z_0 term is the distance from the phased array to the cap's boundary where z is to be determined and z_0 is the correctional value obtained by the method mentioned in the previous paragraph.

A total of seven evenly spaced temporal locations had been selected to be scanned. Once the data is separated, it is ready to be filtered, imaged, and processed for line detection and nugget measurements.

5.2 Image filtering

Filtering an image serves several purposes depending on the context and desired outcome. For this research, the use of filtering an image is to emphasize the signature features previously represented in figure 4.1 while diminishing noise present within the image to enhance the ability to detect these features and thus increase weld detection. The method of filtering used to do so was convolution filtering.

In image processing, convolutional filtering is a technique used to modify images by applying a small matrix called a kernel to each pixel of a 2D array or image. The kernel acts as a window that slides over the input data, performing a mathematical operation called convolution at each position. The process involves multiplying the corresponding elements of the kernel with the elements of the input array covered by the kernel window and summing up the products. By sliding the kernel window over the entire input array and repeating the convolution operation, a new 2D array called the filtered image is generated.

The general expression of a convolution is:

$$g(x,y) = \omega * f(x,y) = \sum_{i=-a}^{a} \sum_{j=-b}^{b} \omega(i,j) f(x-i, y-j)$$

$$(5.2)[27]$$

where g(x,y) is the filtered image, f(x,y) is the original image and ω is the kernel filter.

The kernel design plays an important role in determining the type of filtering being applied. Different kernel matrices produce different effects on the image. For example, blurring or smoothing filters average the pixel values within the kernel window, resulting in a blur or smoothing effect. Sharpening filters enhance the edges and details in an image by emphasizing the differences between neighboring pixels. Edge detection filters highlight the boundaries between different regions in an image by detecting rapid changes in pixel values. For the data presented within this research, many different filters were experimented to enhance line detection within the image and as a result, two different filters were used that produced desirable outputs.

The signature features that yielded the greatest difficulty in detection were the top and bottom liquid steel pool lines. Within the M-scans, one source of difficulty is the presence of the reflection from the boundary between the copper cap and the steel plate. As this is a dry coupled boundary, it is often present at a far greater amplitude than the reflection from the molten pool. This can be seen by the horizontal lines present in figure 5.2 on the left. The first filter that was used to reduce these horizontal lines was a vertical Sobel filter.[27] In figure 5.2 below, the effects of the Sobel filter on the liquid lines of an M-scan can be observed.
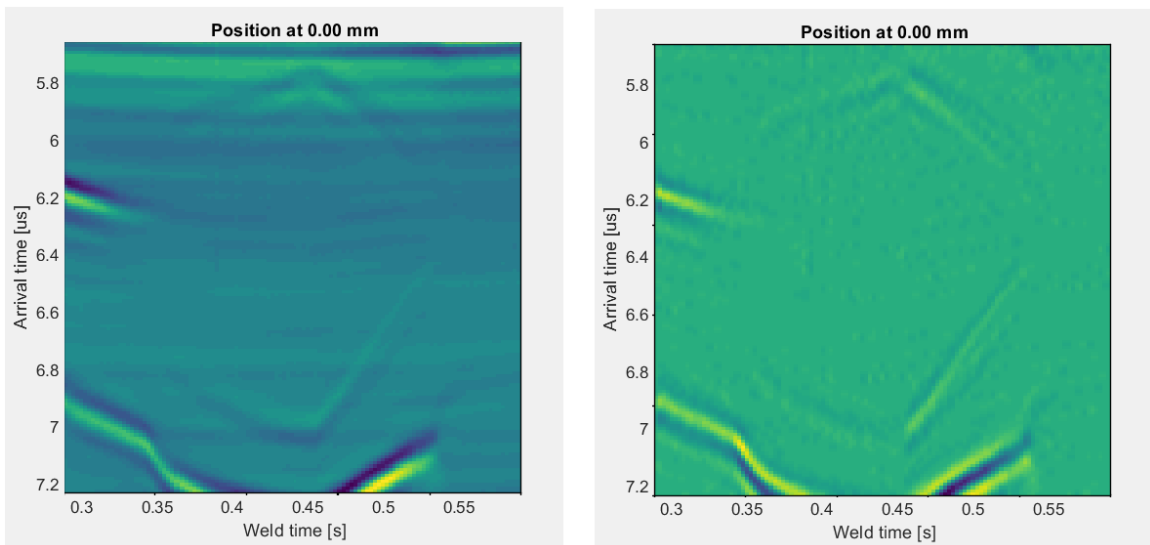
Figure 5-2 The unfiltered image (left) can be seen to have horizontal lines present increasing the difficulty to distinguish signature lines. The filtered image (right) is seen to have enhanced diagonal features while diminishing horizontal ones.

The Sobel filter used is shown in equation 5.3.[27]

$$\begin{bmatrix} -1 & 0 & 1 \\ -2 & 0 & 2 \\ -1 & 0 & 1 \end{bmatrix} \quad (5.3)$$

After implementing the Sobel filter, another filter was used that enhanced diagonals with a negative slope. Since this would only enhance half the liquid lines, a windowing approach was used to split the liquid lines up into sections where each section was then flipped, if necessary, to manipulate the liquid lines so that they were oriented with a negative slope. This filter used is shown in equation 5.4 and its effects for the bottom right liquid line can be seen in figure 5.3.

43

$$\begin{bmatrix} 1 & 0 & -1 \\ 0 & 1 & 0 \\ -1 & 0 & 1 \end{bmatrix} \quad (5.4)$$
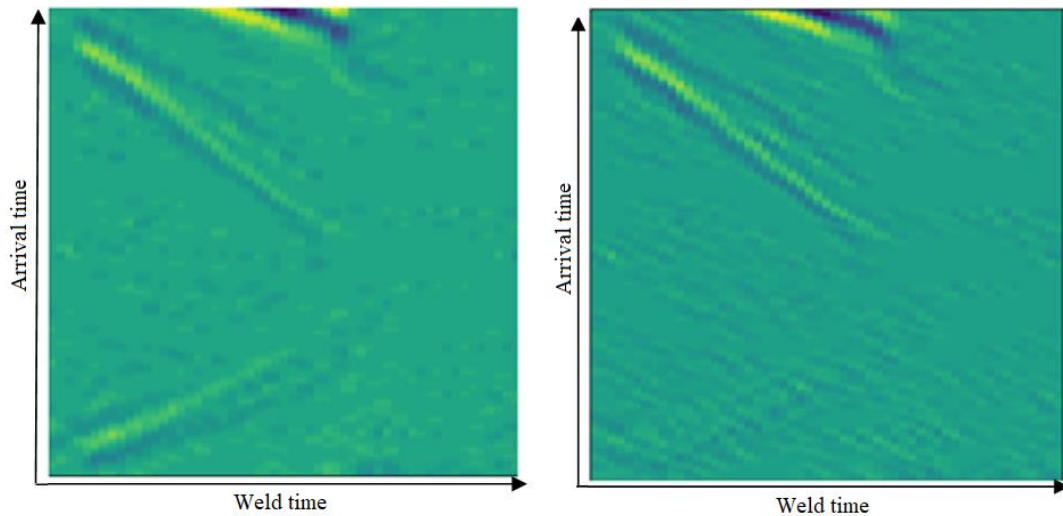
Figure 5-3 The unfiltered image (left) and the filtered image (right). The filtered image can be seen to have an enhanced liquid line. Note that the image shows the bottom right liquid line of figure 5.1 but has been flipped to achieve a negative slope, hence the arrival time axis has also been inverted .

5.3 Line detection and nugget measurement

To be able to measure a nugget's diameter, one must first be able to distinguish whether a weld is present at the temporal locations. If welds are present at adjacent locations, then one can infer that the weld spans between these locations. A way to be able to detect the presence of a weld is to manually look to see if the signature weld's features discussed in figure 4.1 are present across the scans. The approach taken within the research is to develop an automated process to detect the presence of these features. Since this approach will be using a greedy algorithm, ordered conditions will be applied to these detected lines to avoid potential incorrect solutions. If enough features are detected, then the location can be said to be welded. These results will then be compared with manual results and results obtained from other forms of testing.

The front plate interface is the first reflection present within the imaging region. Within the array of data, all reflections detected are stored as values greater than zero. Due to the nature of the setup, the front plate would harbor the strongest reflection in the M-scan because the propagating wave's energy decreases throughout the medium. Within

the array of data, this first reflection can be found where the values are at a maximum. A line can be traced by locating these peak values along the columns of the array.

Additional conditions are applied to avoid incorrect solutions. These conditions would be that the length of the detected line is equal to the number of columns within the array and the variance of the line's position does not exceed too many rows. This first condition arises from the fact that the front plate reflection should be present throughout the entire image while the second condition arises from the fact that the front plate's position has very little variance. The only variances that may arise is from heating of plates that alter acoustic impedances and any expulsion that may occur. When an expulsion occurs, physical parts of the metal are expunged from the environment affecting the quantity of metal present and thus a sharp variance can be seen. When the front plate is located, the image can be cropped and positioned so it is always located at the same position within the image for every scan. This will allow for consistent detection of the back plate and plate separation for every scan.

Detection of the back plate and plate separation were possible because the thicknesses of the plates were known. Prior to the application of current, their positions would not change with respect to the front plate so the starting position in the image where these features are present can be solved for as the speed of the wave within the media is also known. A line detection algorithm was then used by starting within the correct region of data and applying a search window to trace along the array for nearby positive values.

When dealing with the plate separation, a priority is set to search for adjacent elements with a secondary priority in the downward diagonal direction. The reason behind this comes from the nature of how the plate separation is seen to behave in the M-scans. In a successful weld the plate separation disappears shortly after the current is turned on as liquification of the plates start to occur. The condition that is applied to ensure that the plate separation is detected is the length of the detected line must not exceed too far past the position at which current is turned on. The position at which current is turned on can be determined by observing at which position the rows start to vary in the detected line.

When dealing with the back plate a similar approach is taken except the search window takes a priority in the upwards direction when the current is turned off. The position at which this occurs can be determined when the search window starts to consistently store values from that direction. There are instances where the back plate can no longer be seen shortly after the current is turned off, but a successful weld is still performed so the only condition applied is to ensure that the length of the back plate line is greater than or equal to the position at which the current is turned off.

The last feature that needs to be detected within the image is the liquid lines present while the liquification of the plates occurs. These liquid lines can be seen within the image due to the impedance mismatches between the solid and liquid metal. As more of the metal starts to liquefy and penetrate deeper into the plates, the reflection that arises starts to approach the reflections of the plates. This can be seen as the plate separation starts to disappear and a forking feature starts to occur. The approach taken to detect these liquid lines is to crop the image to search within the area where these lines are present. For the research presented, the search window stayed consistent for each set of data because the welding time did not change, but this area can be approximately determined as the rectangle formed between the position at which the disappearance of the plate separation occurs, position slightly past the current off position, the position slightly past the front plate line detected and slightly below the back plate line detected.

With the search window selected it is then split off into four sections where each liquid line is individually detected. The way the search window is split off is along the last row that the plate separation line is positioned and the column at which the current is turned off. As mentioned previously, each section is then oriented in a way where the liquid line has a negative slope, a filter is applied, and then a line detection algorithm is applied. The conditions that are applied to the detected liquid lines are that their slope must not be too close to zero and their R-squared value should be at least 75 percent. These two conditions help decrease false positives. With a tighter window selection and optimized filter, a third condition can be applied in the future where the liquid lines at the top and bottom must intersect or have a reasonable trajectory to intersect. The code for the detection of these features and filtering of the images was written in Python and can

be found in the appendix (Code A:2). An example of these features being detected is displayed in figure 5.4.

When all the features are detected and conditions passed, the weld is determined to be present at that location. In the scanning axis there are a total of seven evenly spaced scans that occur over a span of 5 mm. Therefore, if two adjacent locations are determined
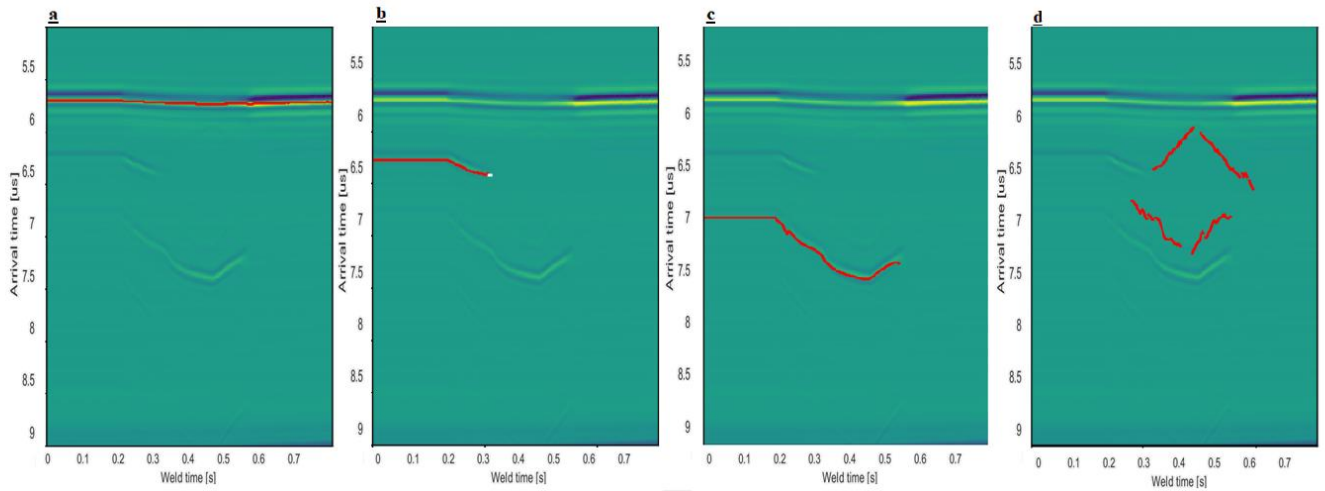
Figure 5-4 Image a) depicts the detection of the front plate. b) depicts the detection of the plate separation line. c) depicts the detection of the back plate, and d) depicts the detection of the liquid lines.

to have a weld present, it can be inferred that the metal is welded throughout the region encompassed, which is a length of $0.8\overline{3}$ mm. To measure the diameter of the nugget that is formed, a simple code that uses the number of adjacent welds detected within a weld's data and the length between two adjacent locations is used. This code was written in Python and can be found in appendix (Code A:3). When the weld is identified in both adjacent scans, it indicates that the object exists at least within the region encompassed by the adjacent scanning locations. To account for the uncertainty of whether the nugget extends up to the next scanning location or not an error is considered. This error is equal to twice the distance between the scanning locations, which in this case would be $+1.\overline{6}$ mm. By assuming the worst-case scenario, where the object reaches just before the next scanning location, this error encompasses any potential variation in the nugget's size or position.

5.4 SAM quality inspection method

With destructive testing methods discussed in chapter 2, the last form of testing to be discussed is the scanning acoustic microscope. The use of a SAM is a non-destructive testing method to evaluate the quality of resistance spot welds. The method involves sending high-frequency sound waves into the weld and measuring the reflection of the sound waves from the plate-plate interface with a transducer. The electrical signals produced by the reflected waves can be used to create an image and evaluate the quality of the weld. Note that in a SAM scan, darker regions signify that weaker reflections were measured while lighter regions signify stronger reflections.

An image of a SAM scan can be seen in figure 5.5 below. Note that the scan has a size of 10 mm along both axes.
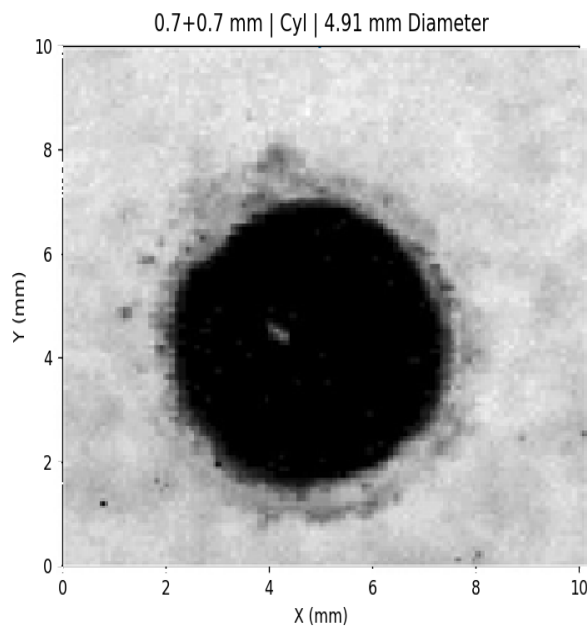
Figure 5-5 An acoustic microscope scan taken of a spot weld. The user can visually identify the boundaries of the weld nugget.

A brief overview of the process is as follows:

1. Sample Preparation: The spot weld sample is typically prepared by cleaning the surface and ensuring it is free from any contaminants that could affect the acoustic wave transmission. Prior to placing the sample into the water bath, it

is also hit with a force to potentially break up the sample is then positioned appropriately for scanning.

2. Scanning Process: The SAM generates high-frequency sound waves, typically in the ultrasonic range, and directs them towards the spot weld. In order to focus the sound waves to the target region where the weld is present, the user must first determine the appropriate depth. This is achieved by examining a region of the data that is not welded, allowing the user to identify the reflection caused by the separation of the plates. The user sets the gates of the SAM to this depth so that when the SAM is placed over the welded region, no reflection is observed, indicating the presence of a welded region. The sound waves penetrate the sample and are partially reflected at the interfaces within the weld. The reflected waves are captured by a transducer, which converts them into electrical signals.

3. Image Formation: The electrical signals obtained from the transducer are processed to create an image of the spot weld. The image represents the internal structure and boundaries of the weld, including the nugget diameter.

4. Nugget Diameter Measurement: Within the SAM image, the operator can visually identify the boundaries of the weld nugget. Using specialized software or measurement tools, the operator measures the diameter of the nugget by selecting appropriate reference points on the image.

5.5 Results and error

Out of 360 welds and 2500 scans, when compared with human analysis, the line detection algorithm managed to obtain the following results displayed in table 5.1 below:

Detection/Plates	0.7 + 0.7 mm	0.7 + 1.6 mm	1.6 + 0.7 mm	1.6 + 1.6 mm
True Positive	110	147	232	145
True Negative	306	286	227	341
False Positive	75	96	51	67
False Negative	136	101	120	77
Detection %	66.03	68.73	72.86	77.14

Table 5-1 Shows the spot weld detection rates for each plate stack combination. It can be seen that the algorithm had greater difficulty in detecting welds that occurred when the thinner plate was closer to the transducer.

By observation the plate combinations where the thinner plate was closer to the transducer resulted in a significantly less successful weld detection. The reasoning behind this is likely due to the increased difficulty in distinguishing the top liquid lines as they're more prone to strong horizontal lines that are present from the copper-plate interface. Note, for the comparison of weld measurements using different methods, manual results for the presence of welds were used.

The raw data collected from the peel test, cross sectional weld cut, phased array scans, and SAM can be found in appendix B. The resulting graphs displayed in figures 5.6-5.11 show the nugget measurement comparisons made using these methods. These graphs were organized according to the geometrical shape of the cap that was used for centered and off-centered welds. With the spot size diameter of the caps used for this research reaching a size of up to 8.80 mm, and the phased array imaging range only spanning a range of 5 mm, some welds presented were off-centre enough that the array system could not scan the entire nugget. Misalignment from the center scanning axis was incorporated into the graphs.
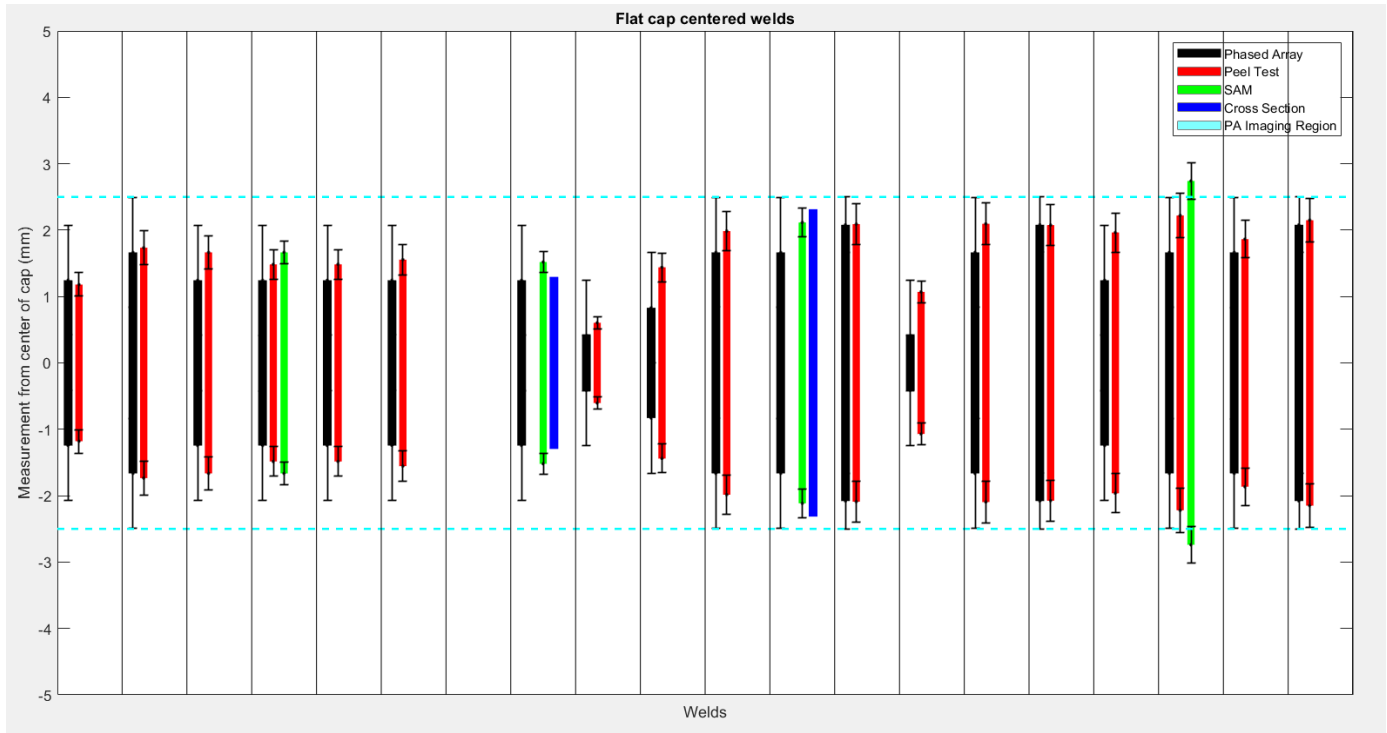
Figure 5-6 A graph showing the comparison between the different measuring methods for 20 flat cap geometry centered welds. It is observed that all the phased array measurements fall within uncertainty of the other measuring methods provided. The resulting cap used to conduct these 20 welds is shown below where the spot weld is concentrated in the center of the scanning axis.
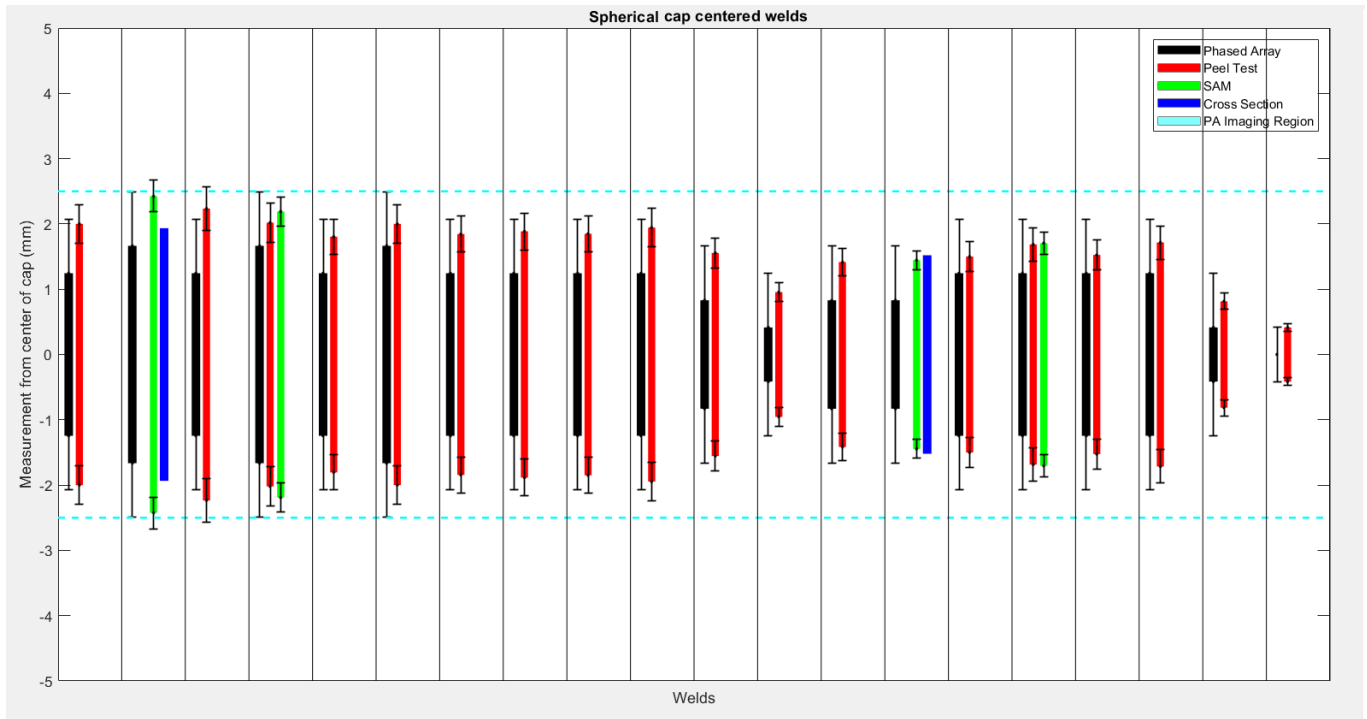
Figure 5-7 20 Spherical cap geometry centered welds are provided above. All the phased array measurements fall within uncertainty of the other measuring methods provided. The cap used for these welds are shown to have residue concentrated in the center which agree with the symmetrical scans observed using the phased array.

52
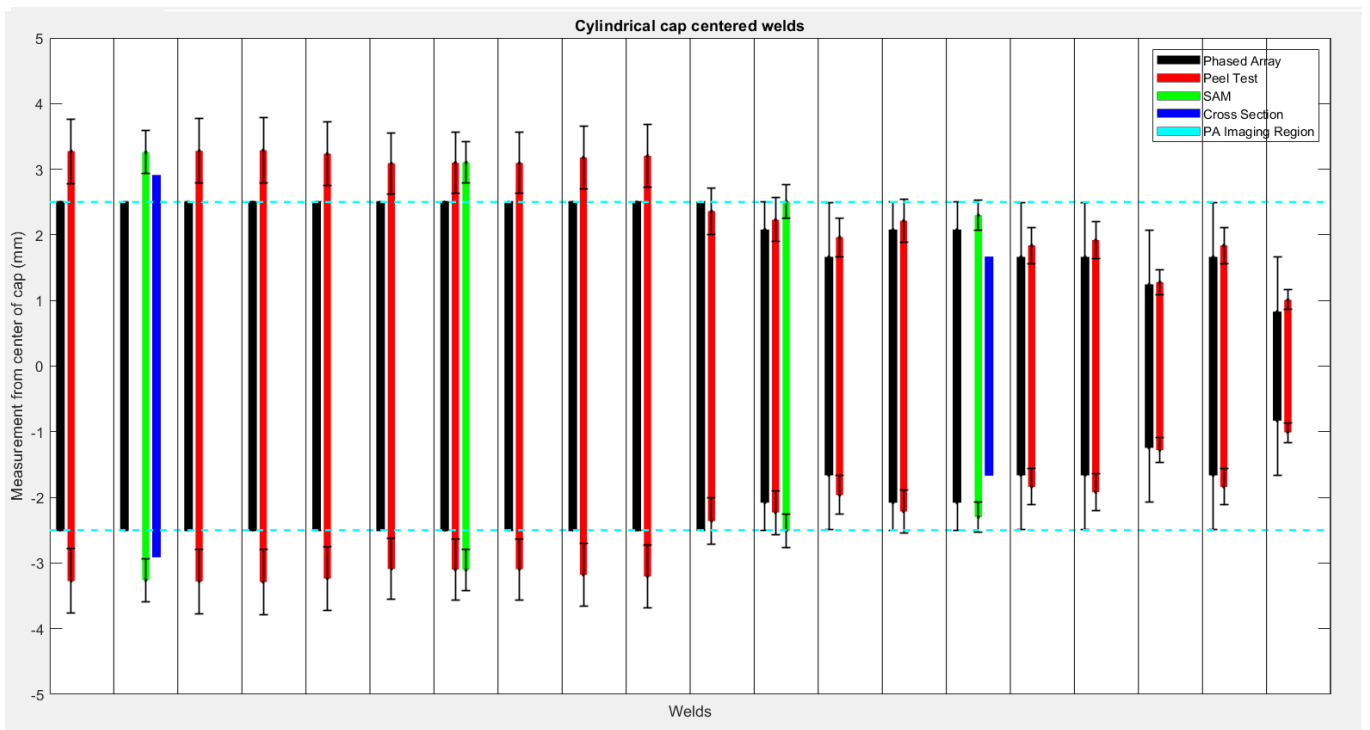
Figure 5-8 Cylindrical cap geometry centered welds are provided above. It is observed that for welds that were centered and exceeded 5 mm in diameter, the phased array provided scans where welds were present in each scan. The results of the caps used for the first half of the welds are shown on the left below and the rest of the half on the right. Welds measuring less than 5 mm were in strong agreement with other measuring methods provided.
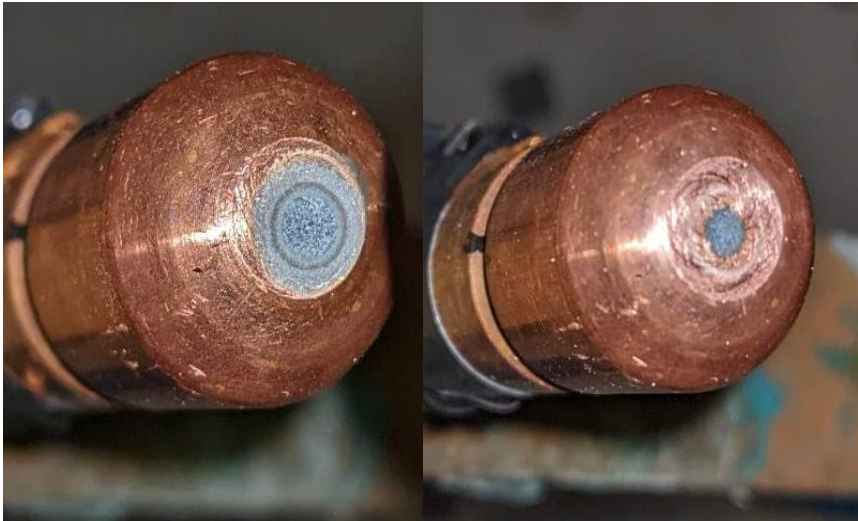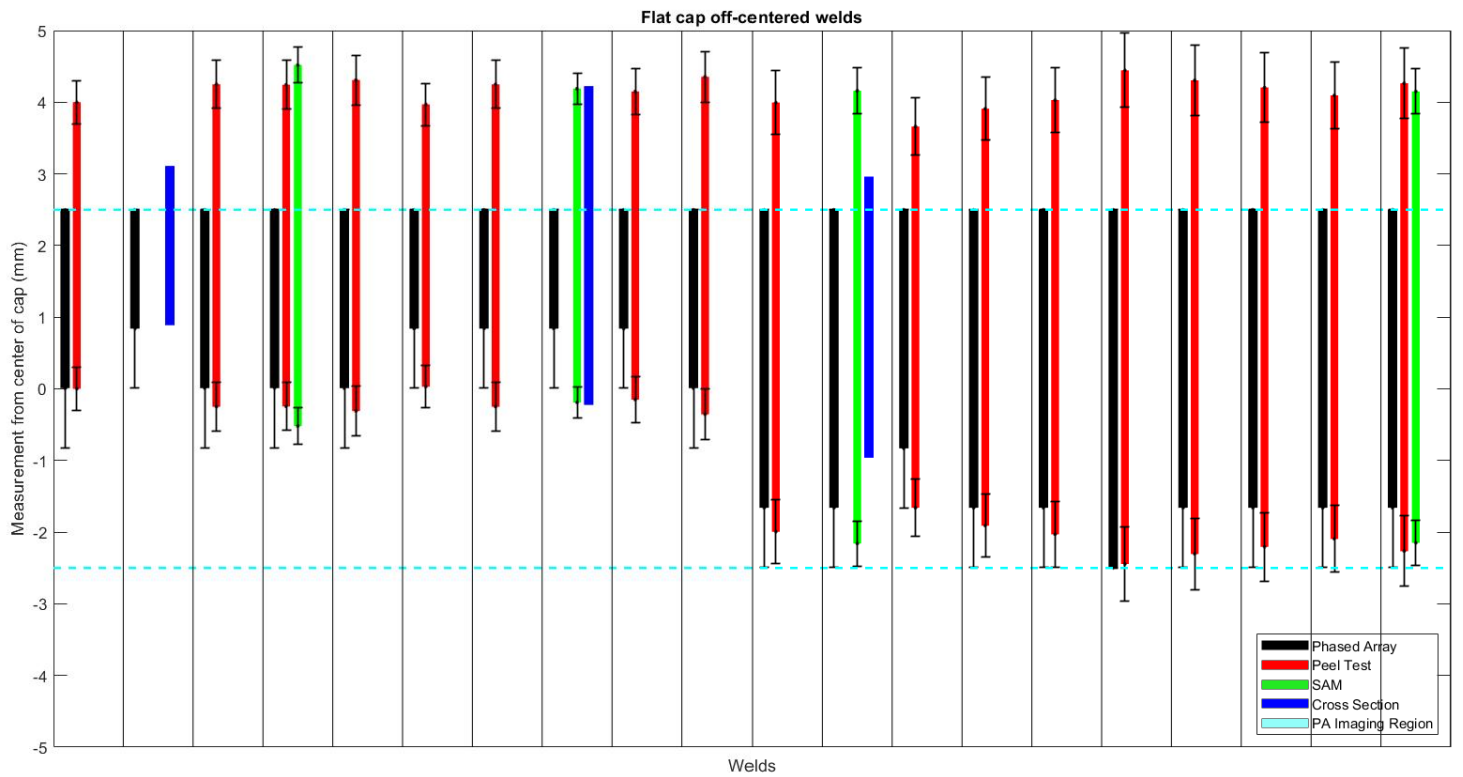
Figure 5-9 Flat cap geometry off-centered welds can be observed. The first 10 welds were performed using the left cap shown with an approximate 2 mm deviation from the center of the cap. The remaining last 10 welds are performed using the right cap provided with an approximate 1 mm deviation from the center scan. The imaging region is enclosed by the red lines provided in the cap images. It is observed that when weld misalignment is accounted for, the phased array data that is observed strongly agrees with the diameter of the nugget exposed in the imaging region.
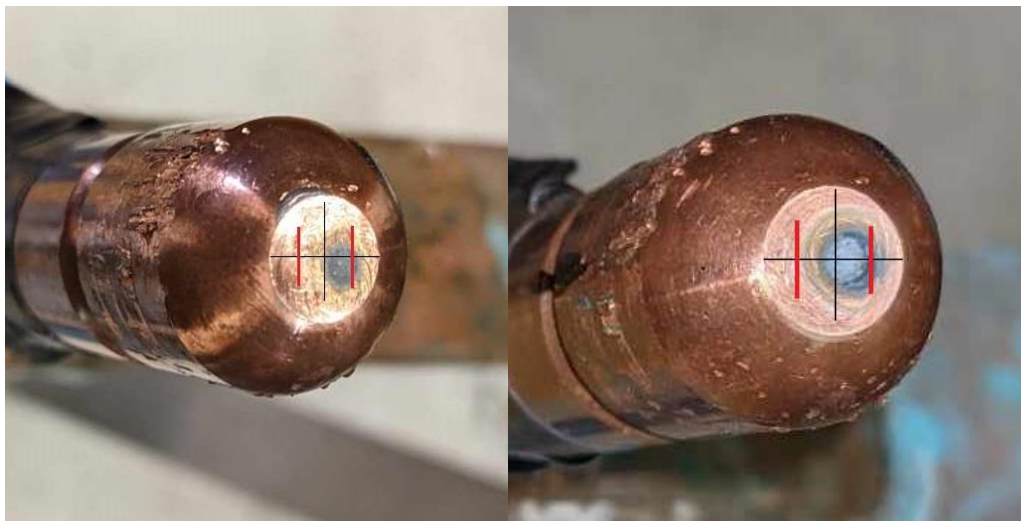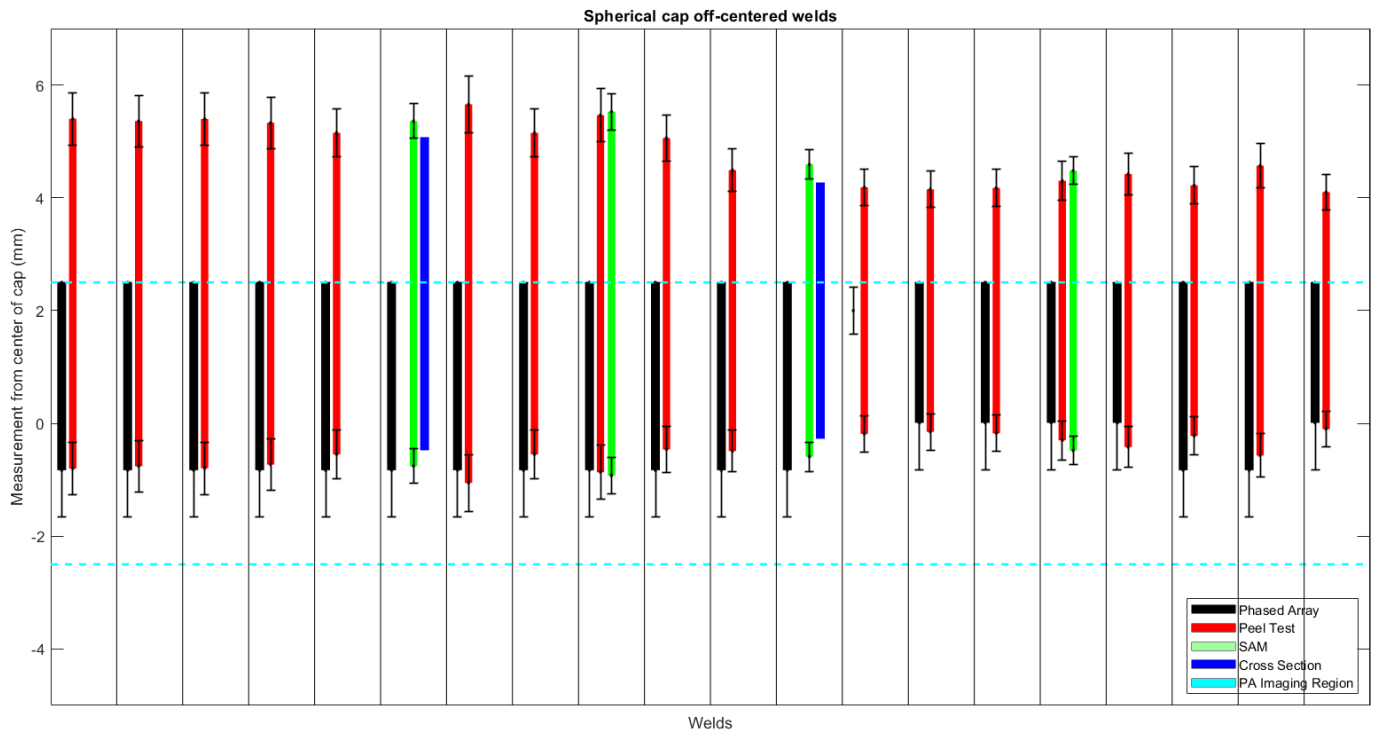
Figure 5-10 Spherical cap geometry off-centered welds show underestimation of the nugget's diameter but when physical deviation from the center of the cap is accounted for, the phased array measurements of the nugget exposed in the imaging region, show great agreement with other measurement methods. The first 10 welds conducted are shown using the left cap's deviation from the center while the right cap shows the remaining 10 welds.
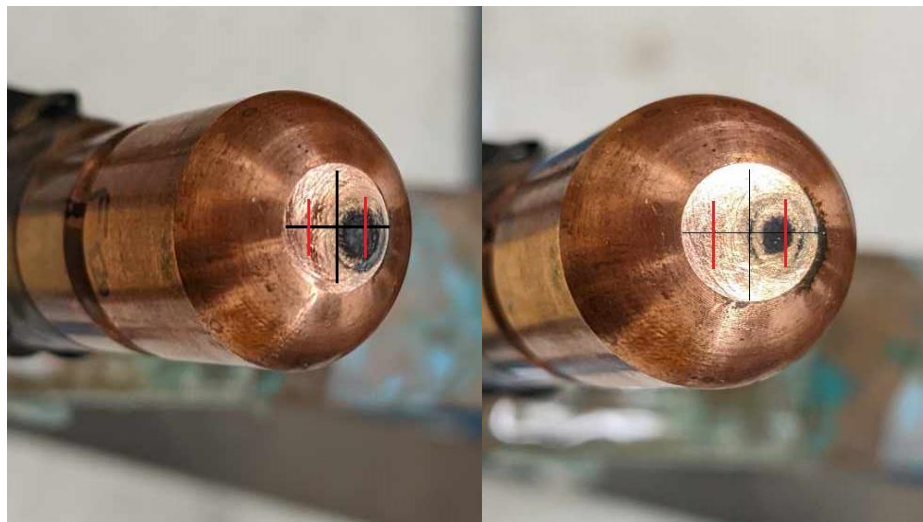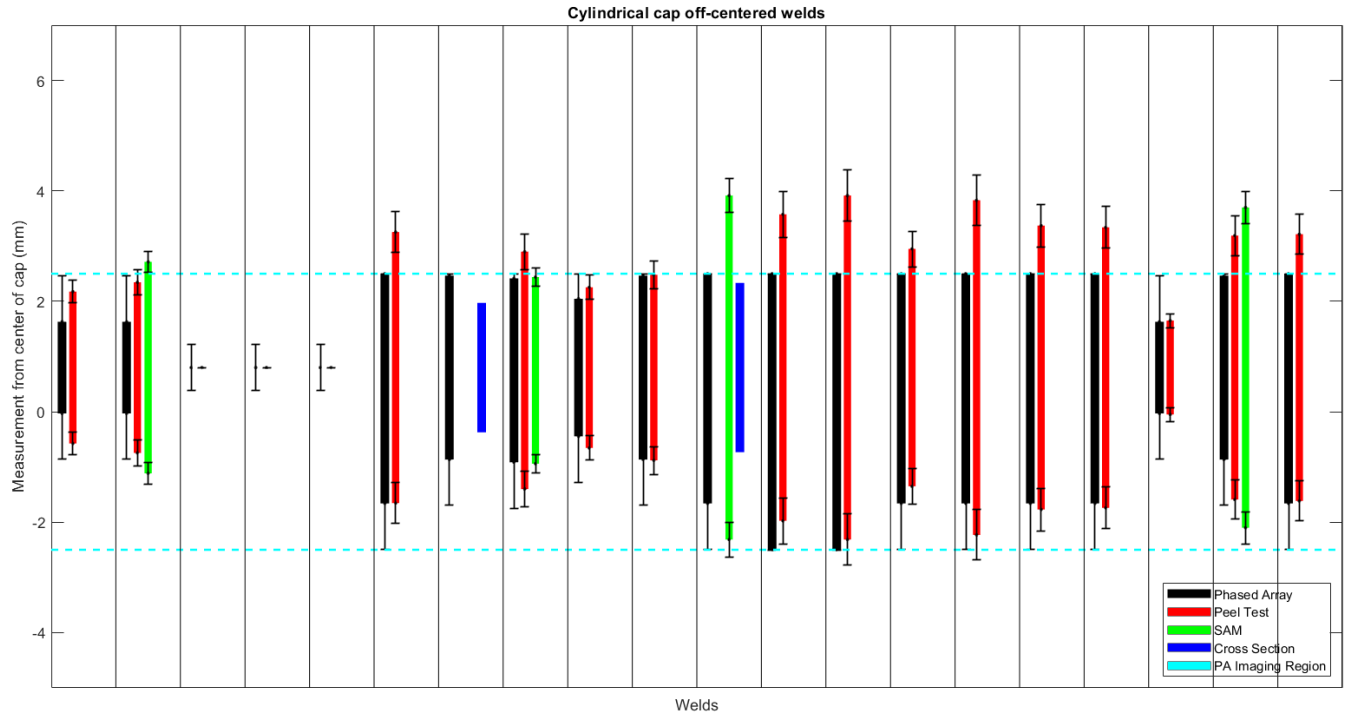
Figure 5-11 Cylindrical cap geometry off-centered welds are shown above. All 20 welds were conducted using the cap shown below. With only a slight deviation from the center, some welds were still entirely contained within the PA imaging region which showed agreement with other measuring methods. For welds that exceeded the imaging region, agreement was still shown for the part of the nugget exposed within the imaging region.

    As previously mentioned, the errors associated with the phased array data points arise from the uncertainty of how far the nugget extends up to the next scanning location. In the case where the weld is not present at the end of the scanning axis, the error is equal to twice the distance between the scanning locations because there is uncertainty on both sides of the nugget. In this case it results in an uncertainty of up to $+1.\overline{6}$ mm. By

assuming the worst-case scenario, where the object reaches just before the next scanning location, this error encompasses any potential variation in the nugget's size or position.

The errors associated with the peel test arise from referencing previous articles that state around a 10 % to 20 % error. For the purpose of this research, an average of 15 % was used. This error mainly comes from the operator's technique. The accuracy of the measurements can be influenced by the skill and technique of the operator. Inconsistent application of the caliper, misalignment of the arms, or variations in the applied pressure can introduce errors in the measured diameter. The surface conditions of the weld can also affect the accuracy of the measurement. Irregularities or roughness of the surface such as bending of the metal near the nugget when the peel is performed may create difficulty in locating the outer edges of the nugget. To mitigate these errors, consistent measurement techniques should be used. Typically, multiple measurements are taken at different locations and an average is used to also mitigate error, but the diameters taken for the welds presented in this research rely on preserving orientation as they must be measured along the scanning axis.

The error associated with the SAM data presented in this research is 10 %. This also arises from operator techniques and image interpretation. The operator's interpretation of the SAM image can introduce some level of subjectivity and potential errors. Differences in how the operator identifies and defines the boundaries of the nugget can affect the measured diameter. To mitigate this error proper training and standardized procedures for image interpretation and measuring should be employed.

To summarize, in figures 5.6-5.8 where the welds conducted were centered with the phased array scanning range, phased array data is in strong agreement with other measurement methods. For figures 5.9-5.11, where misalignment was observed from the phased array imaging center, the phased array data underestimated the diameter measurement of the nugget. Although the diameter was underestimated, when the misalignment from the center was considered, the diameter of the nugget exposed within the phased array imaging region showed agreement with other measurement methods such as the peel test and SAM provided. One thing to note is that the cross sectional weld cuts provided typically underestimated the diameter measurement when compared with

the SAM and peel test. This is expected as the cross sectional weld cuts that are not cut directly through the center of the weld will underestimate the true diameter of the nugget measured.

In figure 5.12, a spherical cap geometry weld performed resulted in the residual region shown. It is observed that the welds are occurring misaligned from the center. This means that the scans should be misaligned when observed, thus underestimating the weld. The M-scans taken from a weld performed using this cap can be seen in figure 5.13 below.
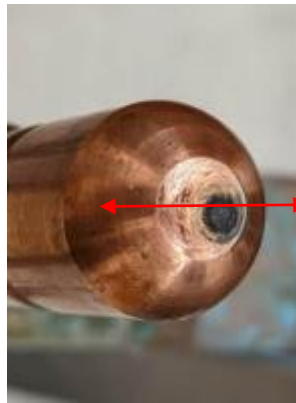
Figure 5-12 The region where welds were occurring on the copper cap for a set of cylindrical off centered welds produced can be seen above. This significantly misaligned weld can be seen by the misaligned scans observed with the phased array. The red line in this picture indicates the scanning axis.
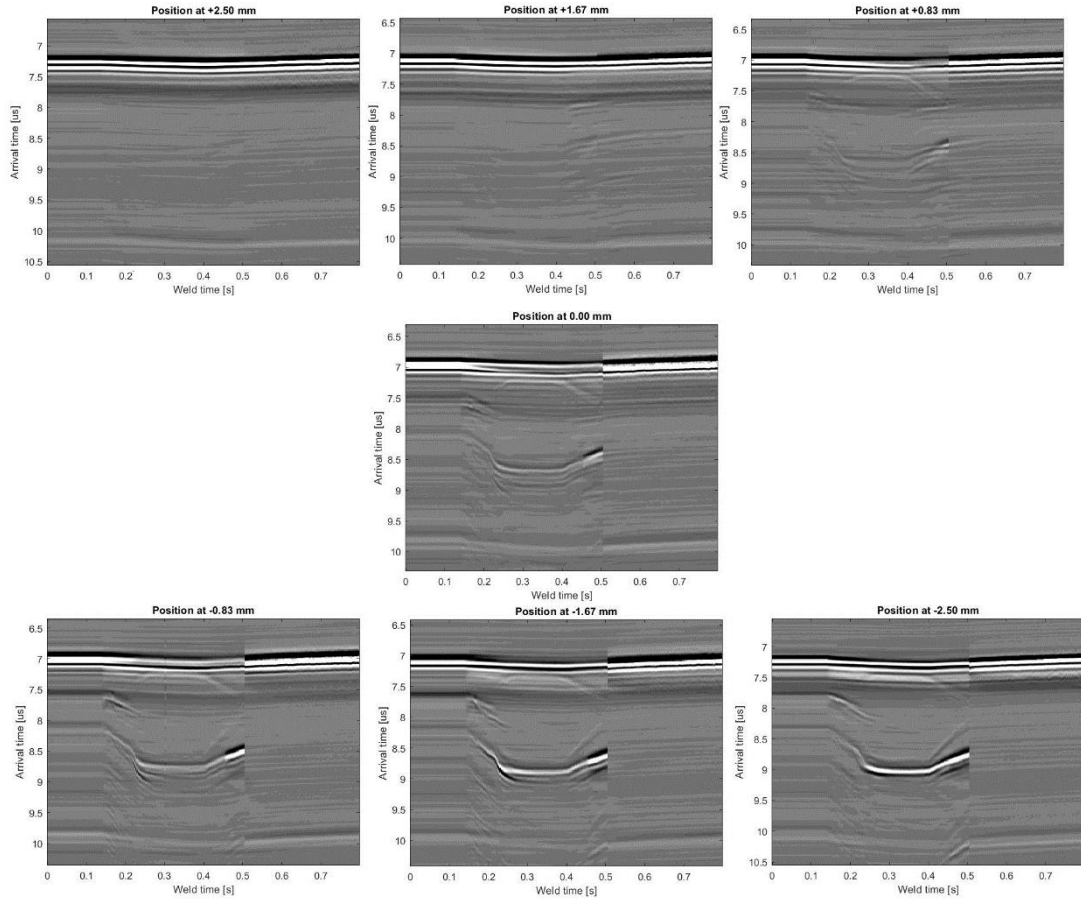
Figure 5-13 The M-scans acquired for a spherical off-centered weld. The scans are misaligned which agrees with the positioning of the misalignment presented on the copper cap in figure 5.12.

On the contrary, when the region where the welds occurred were centered on the copper cap such as the one shown in figure 5.14, the m-scans acquired were symmetrical and the data showed greater agreement with other measurement methods. The cylindrical the m-scans for a weld performed with this cap can be seen in figure 5.15.

Figure 5-14 Copper cap used to weld a set of centered cylindrical. The welds can be seen to be centered, producing centered M-scans such as the one shown in figure 5.15.
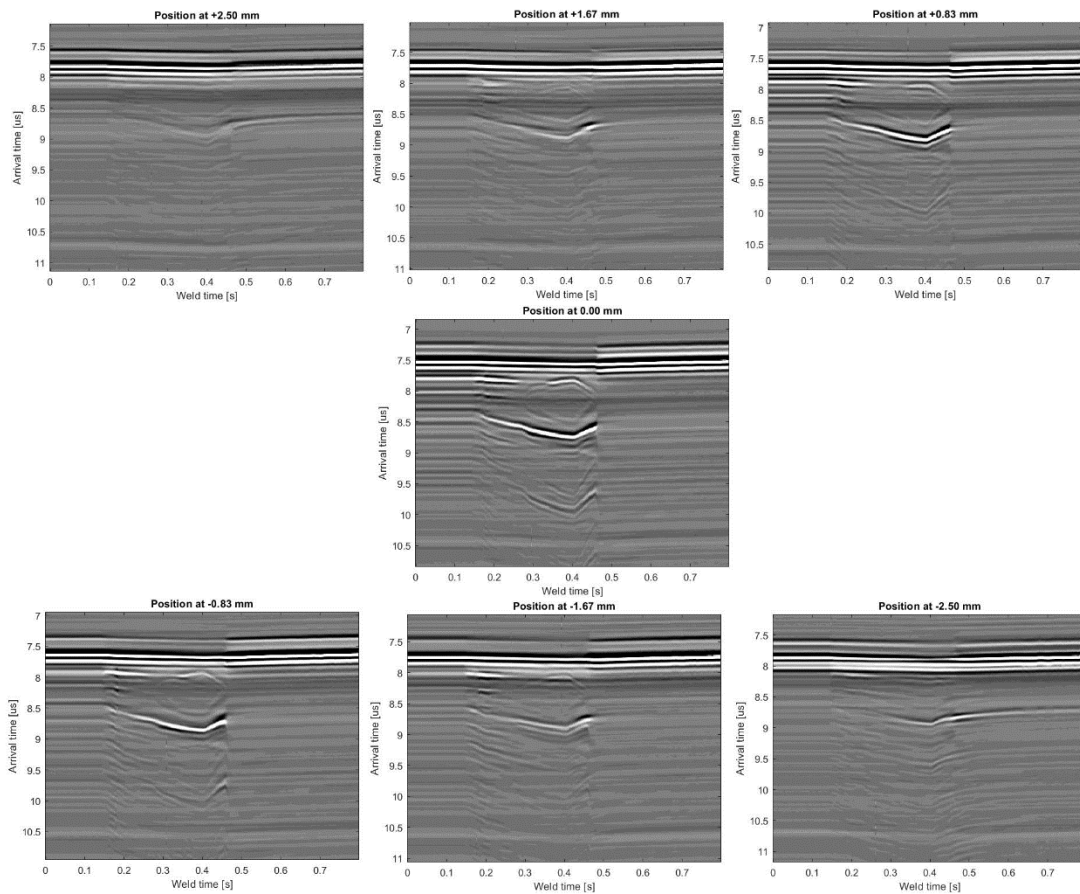
Figure 5-15 The M-scans for a centered cylindrical cap weld performed by the cap shown in figure 5.14. It can be observed that the scans are aligned in the center with disappearance of the weld occurring symmetrically with respect to the center.

Although cross sectional weld measurements are not as reliable as other testing methods as they not only destroy the weld but also commonly underestimate it, additional information can still be extracted. The penetration depths of the welds can be observed and compared with the penetration depths that can be calculated using the phased array scans.

To calculate the penetration depths of the welds using the cross section of the weld, it is a simple matter of taking the ratio of penetration into the weld to the total thickness of the plate with respect to the plate separation position. This can be seen in figure 5.16.
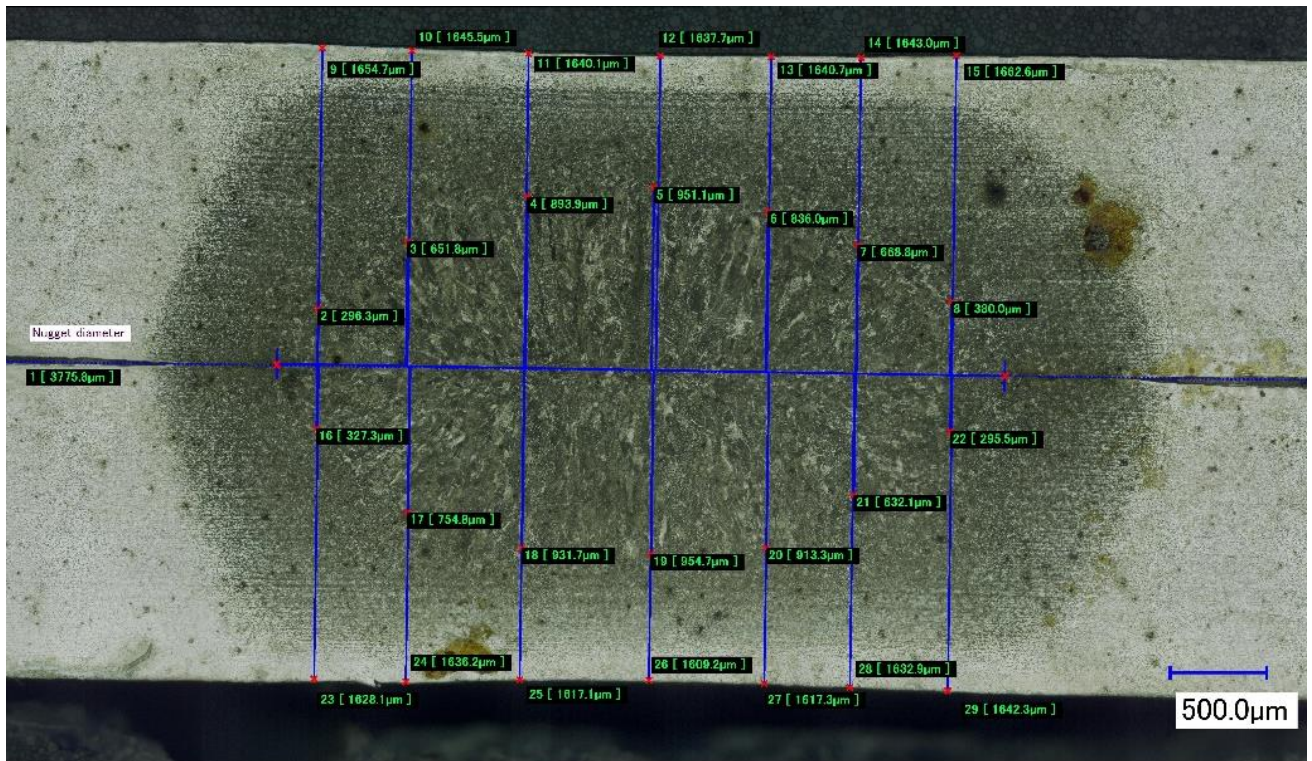
Figure 5-16 Cross section of an off centered spherical weld. The penetration depth can be seen throughout various parts of the weld.

To calculate the penetration depths presented in the M-scans, a different approach must be taken. Due to the presence of the liquid metal and change in heat occurring, the time of flight for the back plate, plate separation and bottom liquid lines will vary over time and thus its position on the M-scans will vary. The position at which the liquid

formation is at a maximum is typically the position at which the liquid lines are the farthest from one another. This usually occurs right before the current is turned off and is the best position to use to calculate these depths, but correctional values must be placed to be able to accurately calculate the depth penetration occurring at that time. In any M-scan, the bottom liquid line and bottom plate are both influenced by the entire liquid metal, so to determine the top and bottom penetration depths with respect to the separation line, the bottom liquid line's correctional position must be determined. This correctional value is equal to the change in the back plate's position. Note that the top liquid line does not need a correctional value because the reflection of the top liquid line is achieved without being influenced by the liquid itself as the wave only travels through solid metal before it reaches this interface. The penetration depth can be calculated with the use of the top liquid line, corrected bottom liquid line value, the initial position of the top plate, plate separation, and bottom plate. A summary of the top and bottom plate penetration depths for each scan acquired for the weld represented in figure 5.16 can be seen in table 5.2 below.

M-scan position (mm)	1 +2.50	2 +1.67	3 +0.83	4 0	5 -0.83	6 -1.67	7 -2.50
Front plate penetration (%)	0	0	0	40	54	64	54
Back plate penetration (%)	0	0	0	36	52	55	59

Table 5-2 Shows a comparison of penetration depths as a percentage between the M-scan positions. Due to misalignment in the weld, no penetration is present from +2.50 mm to +0.83 mm because there is no visible weld observed.

Table 5.3 below shows the penetration depths calculated using the cross sectional image provided in figure 5.16 above:

Cross sectional position	1	2	3	4	5	6	7
Front plate penetration (%)	20	46	58	59	57	39	18
Back plate penetration (%)	18	40	55	58	51	41	23

Table 5-3 Shows the penetration depths of the cross sectional image provided as a percentage.

Note that a misalignment of approximately 2 mm was observed with this weld that was conducted. Thus, a direct comparison between the cross sectional position and M-scan position cannot be made. The first cross sectional position must be compared between +0.83 mm and 0 mm. When these charts are compared this way, the measurements of penetration percentages closely resemble each other in magnitude and shape.

Another example of a weld's cross sectional penetration depths compared with the phased array measurements can be seen below in figure 5.17 and table 5.4. Note that discrepancies can be observed between the two methods being compared. Some reasoning behind these discrepancies may arise from the fact that the weld may have been misaligned in both axes. A misaligned weld along the scanning axis would result in an underestimation of the size of the weld by the phased array method while a misaligned weld along the non-scanning axis would result in an underestimation of penetration depths by the phased array method when compared with the cross sectional penetration depths along the center of the weld. In addition, when measuring the size of the nugget diameter, temperature dependent speed of waves was not considered. This has also contributed to a discrepancy between the two methods in measuring penetration depths. A strong temperature dependent gradient for the speed of waves is present along the

scanning axis, thus for a more accurate result, the TOF should be adjusted based on the temperature profile of the weld, at least to that of a linear approximation.
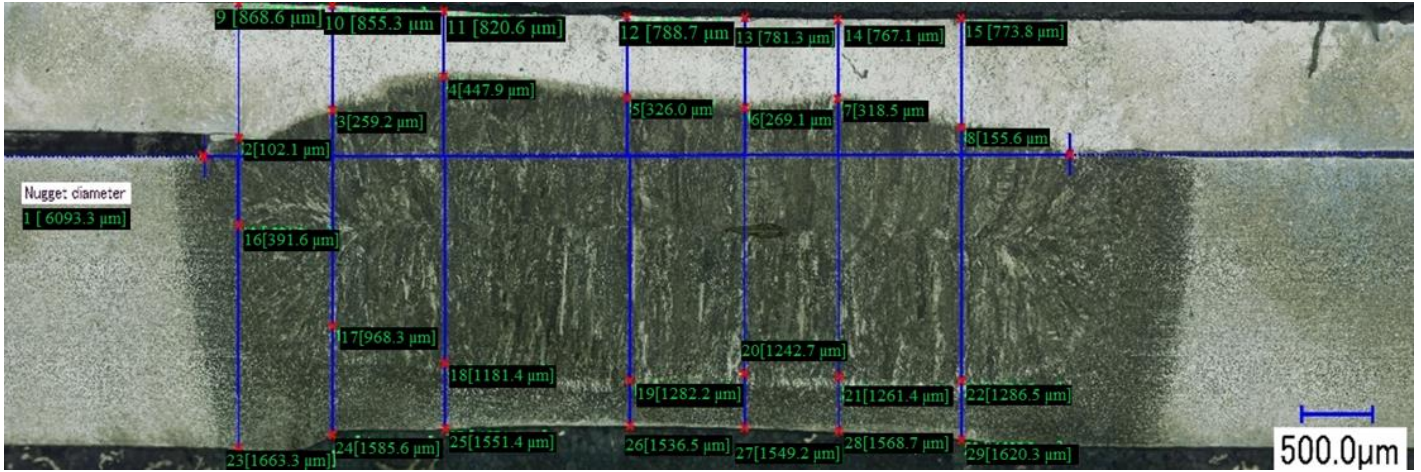
Figure 5-17 Cross section of a weld with differing stack thicknesses. The penetration depths at various instances of the nugget can be observed.

M-scan position (mm)	+2.50	+1.67	+0.83	0	-0.83	-1.67	-2.50
Front plate penetration (%)	0	0	0	6	9	6	16
Back plate penetration (%)	0	58	86	63	84	70	62
Cross section position	1	2	3	4	5	6	7
Front plate penetration (%)	12	30	55	41	34	42	20
Back plate penetration (%)	24	61	76	83	80	80	79

Table 5-4 Penetration depths as a percentage obtained by the cross sectional image of a weld and phased array M-scans. In this instance, when misalignement is taken into account, the back plate seems to show agreement between the two methods while the front plate has a large discrepency. This is likely due to an off center weld along the axis perpendicular to the scanning axis.

In some instances, there are cross sectional weld cuts taken where there were voids present. An image of a void can be seen in figure 5.23. They may arise due to gases being trapped within the molten pool as well as from expulsion sites. In the cross sectional weld cuts performed, voids were found to be present in some of them. Within the M-scan data, no concrete conclusions could be made whether voids could be detected as the voids themselves did not occur along the scanning axis. In the cross sectional cuts where voids were present misalignment had occurred when the weld was performed and if the weld cut did not occur directly through the center of the weld, it may have been underestimated. Therefore, it is unknown whether the voids occurred along the scanning axis.
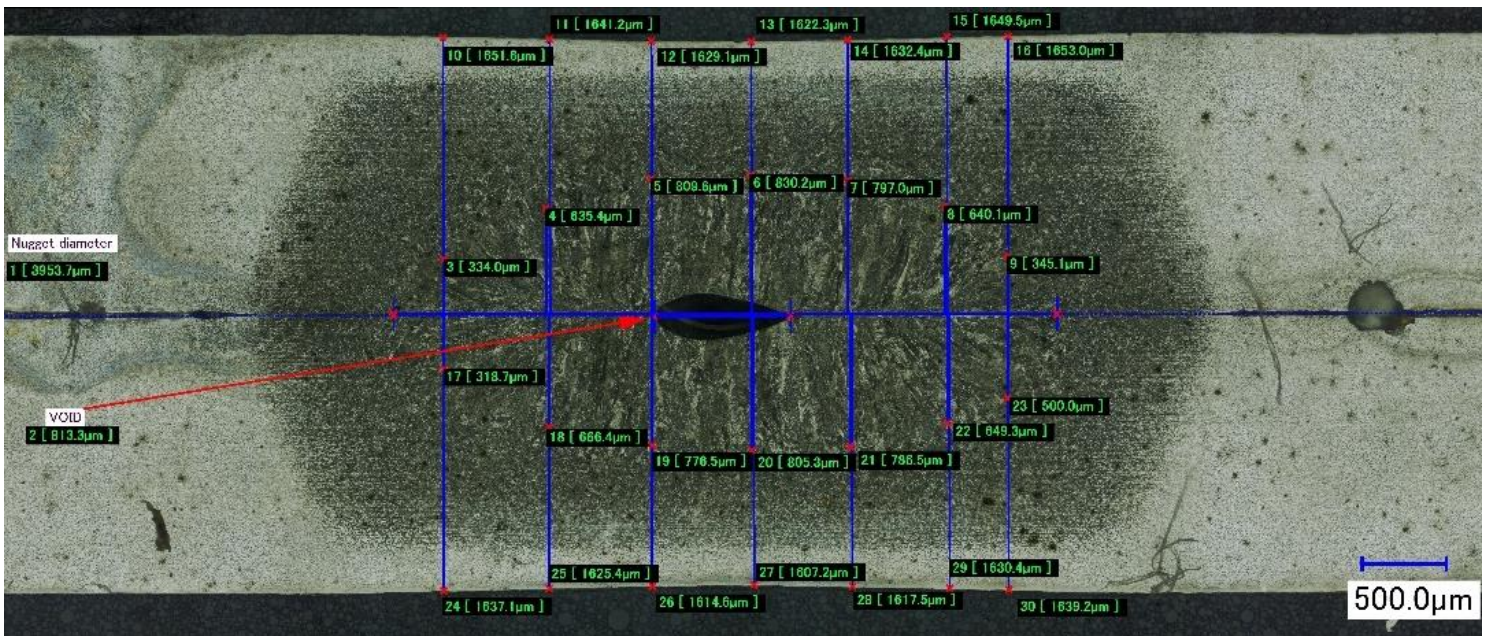
Figure 5-18 A depiction of a cross sectional cut where a void was present and penetration depths can be observed throughout the nugget.

For future testing of presence of voids, a more controlled environment where the welds occur should be employed. This can be done so by limiting the spot size of the copper cap to exactly 5 mm, which matches the span over which the array scans. The welds performed within this thesis had spot sizes ranging from 8.15 mm to 8.65 mm as caps were dressed between data sets to avoid variability occurring from buildup of residue.-

5.6 Conclusions

Misalignment was readily detected in welds by observation of misalignment in M-scans. Theoretically, this should also extend to the ability to detect irregular weld shapes, provided they occur along the scanning axis. Conclusions on voids cannot be made as not enough data is present and misalignment of the weld resulted in the inability to determine whether the scanning axis occurred along the presence of the voids that were available. In instances where there was no misalignment present, weld nugget measurements were in strong agreement with other testing methods. While underestimated nuggets by phased array appear to be a result of misalignment. This misalignment is evident through the positioning of the weld residue left on the copper cap in addition to strong weld presence predominantly shown on one end of the M-scans. In terms of cap performance, all three welds were able to detect the presence of welds and by extension measure nugget diameters when the welds performed were centered on the copper cap. Although the drawback of the cylindrical cap is positioning along the scanning axis is necessary as misalignment with the scanning axis will produce poor quality M-scans. Since geometrical caps don't influence the quality of M-scans obtained, the best geometrical cap to use would be the spherical one as it is the cheapest to reproduce. In the case of determining penetration depths at different areas of the weld, the penetration depths calculated using the phased array M-scans appear to follow a similar pattern with the penetration depths calculated using the cross sectional cuts. Additional data where the weld and cross sectional weld cut is centered is necessary to confirm theory. The results show the possibility of measuring nugget diameters along the scanning axis with the ability to detect misalignments.

CHAPTER 6
SUMMARY AND FUTURE WORK

In this research, significant progress was achieved in the evaluation and detection of various parameters in resistance spot welding. The findings and accomplishments can be summarized as follows. The study successfully detected welds throughout different locations along the nugget with the phased array, resulting in the ability to measure nugget diameters using three different cap geometries, with the flat cap demonstrating the most effective performance.

Evaluation of penetration depths showed that measurements obtained from the phased array system, although differing slightly, appeared to follow pattern with those derived from cross-sectional weld cuts, indicating a potential method of measurement.

Misaligned welds were successfully identified, which is crucial for assessing the quality of spot welds. Voids, however, were not detectable in the M-scans due to the misalignment of scans and welds. The detection algorithm proved effective in identifying the front plate, back plate, and plate separation. Challenges were encountered in measuring the liquid lines, particularly when thin plates were used.

Comparative analysis revealed that centered welds conducted using the phased array method fell within the expected error range when compared with other testing methods such as the peel test, validating the reliability of the approach.

Building upon these achievements, several suggestions for future work can be proposed to further enhance the capabilities and applicability of the phased array system in weld evaluation and quality assessment.

To improve void detection, it is recommended to generate additional data where the cap's spot size matches the scanning axis range. This approach ensures that the welds occur in the center of the scanning axis, significantly increasing the likelihood of void occurrence and facilitating the possibility of void detection using phased array techniques.

Enhancing the detection algorithm is essential for better performance. Tighter windowing techniques can be implemented to enhance the detection of liquid lines. Exploring different filtering approaches could also be beneficial in improving the quality of M-scans and enhancing detectability. As welds are typically performed within a 1.0-1.5 s window, a decision of the weld quality must occur within that time, so optimization of this process is essential.

The integration of artificial intelligence (AI) techniques holds promise in advancing feature detection and measurement accuracy in spot welding. AI algorithms can potentially overcome challenges related to distinguishing features, especially in cases involving thin plates. Research within our group is currently performing the implementation of AI in detecting these signature weld features.[27]

Conducting material testing is crucial to evaluate the effectiveness of measuring welds using different materials, such as aluminum. This analysis will provide valuable insights into the phased array's performance across various material types.

By addressing these future work suggestions, the research aims to advance the capabilities, accuracy, and practicality of the phased array system for spot weld evaluation, making it more suitable for production-ready deployments in the automotive industry.

REFERENCES/BIBLIOGRAPHY

[1] Ghaffari, B., & Mozurkewich, G. (2010). "Non-destructive evaluation of spot-weld quality. Failure Mechanisms of Advanced Welding Processes", 101–136. doi:10.1533/9781845699765.101

[2] Karloff, Anthony C. (2013). "Real-time Expulsion Detection and Characterization in Ultrasound M-scans of the Resistance Spot Welding Process." Electronic Theses and Dissertations, 4735. Retrieved from https://scholar.uwindsor.ca/etd/4735

[3] Agashe, S., & Zhang, H. (2003). "Selection of schedules based on heat balance in resistance spot welding. Welding Journal", 82, 179S-183S.

[4] Duraivelan, D., Murugesan, R., & Ramprasath, B. (2018). "Investigation on strength of resistance spot welding joint of copper and brass using various filler materials." IOP Conference Series: Materials Science and Engineering, 402, 012189. doi:10.1088/1757-899x/402/1/012189

[5] Olympus Panametrics. (n.d.). "UT technotes" [PDF file]. Retrieved from https://www.olympus-ims.com/data/File/panametrics/UT-technotes.en.pdf

[6] Engineering Toolbox. (n.d.). "Speed of Sound in Solids." Retrieved from https://www.engineeringtoolbox.com/sound-speed-solids-d_713.html

[7] Ouellette, Andrew. (2015). "Analysis of the Effect of Thermal Gradients on the Real-time 2D Imaging of the Spot Weld Process." Electronic Theses and Dissertations, 5317.

[8] Iowa State University Center for Nondestructive Evaluation. (n.d.). "Speed of Sound in Solids." Retrieved from https://www.nde-ed.org/Physics/Sound/speedinmaterials.xhtml

[9] Norton, M. P., & Drew, S. J. (2001). "VIBRATION GENERATED SOUND | Fundamentals." Encyclopedia of Vibration, 1443–1455. doi:10.1006/rwvb.2001.0207

[10] White, P. J., Clement, G. T., & Hynynen, K. (2006). "Longitudinal and shear mode ultrasound propagation in human skull bone. Ultrasound in Medicine & Biology", 32(7), 1085–1096. doi:10.1016/j.ultrasmedbio.2006.03.015

[11] Aabid, A., Raheman, M. A., Ibrahim, Y. E., Anjum, A., Hrairi, M., Parveez, B., Mohammed Zayan, J. (2021). "A Systematic Review of Piezoelectric Materials and Energy Harvesters for Industrial Applications. Sensors," 21(12), 4145. doi:10.3390/s21124145.

[12] Hedrick, W. R., & Hykes, D. L. (1996). "Beam Steering and Focusing with Linear Phased Arrays." Journal of Diagnostic Medical Sonography 12(5), 211–215. doi:10.1177/875647939601200502

[13] Nave, R. (n.d.). "Huygens' Principle." HyperPhysics. Georgia State University, Department of Physics and Astronomy. Retrieved from http://hyperphysics.phy-astr.gsu.edu/hbase/phyopt/huygen.html

[14] Acebes, M., Flórez, D., Thorpe, N., & Aguado, M. (2015). "Optimization of phased-array transducers for ultrasonic inspection in composite materials using sliding probes." 6th International Symposium on NDT in Aerospace 2014, 12-14th November, Madrid, Spain. e-Journal of Nondestructive Testing Vol. 20(1). https://www.ndt.net/?id=16966

[15] Ng, A., & Swanevelder, J. (2011). "Resolution in ultrasound imaging. Continuing Education in Anesthesia Critical Care & Pain", 11(5), 186–192. doi:10.1093/bjaceaccp/mkr030

[16] Chertov, A. M., Karloff, A. C., Perez, W., Lui, A., & Gr Maev, R. (2012). "In-process ultrasound NDE of resistance spot welds. Insight - Non-Destructive Testing and Condition Monitoring", 54(5), 257–261. doi:10.1784/insi.2012.54.5.257

[17] Lui, A, "Development of an Ultrasonic Linear Phased Array System for Real-time Quality Monitoring of Resistance Spot Welds" (2012). Electronic Theses and Dissertations. 4826. https://scholar.uwindsor.ca/etd/4826

[18] Tortoli, P., Bassi, L., Boni, E., Dallai, A., Guidi, F., & Ricci, S. (2009). "ULA-OP: an advanced open platform for ultrasound research". IEEE Transactions on Ultrasonics, Ferroelectrics and Frequency Control, 56(10), 2207–2216. doi:10.1109/tuffc.2009.1303

[19] Company: AOS Advanced OEM solutions. (n.d.). Retrieved from https://www.aos-ndt.com/

[20] Chertov, A. M., Karloff, A. C., Perez, W., Lui, A., & Gr Maev, R. (2012). "In-process ultrasound NDE of resistance spot welds. Insight - Non-Destructive Testing and Condition Monitoring", 54(5), 257–261. doi:10.1784/insi.2012.54.5.257

[21] Haber, H. (2009). "Fermat's principle in action [PDF document]." Retrieved from http://scipp.ucsc.edu/~haber/ph5B/fermat00309.pdf

[22] "Piezoelectric transducer." (2020, June 26). Retrieved from https://electricalbaba.com/piezoelectric-transducer/

[23] Yu, H. (2020). "Scanning acoustic microscopy for material evaluation. Applied Microscopy", 50(1). doi:10.1186/s42649-020-00045-4

[24] Baad, M., Lu, Z. F., Reiser, I., & Paushter, D. (2017). "Clinical Significance of US Artifacts. RadioGraphics", 37(5), 1408–1423. doi:10.1148/rg.2017160175.

[25] Denisov, A. A., Shakarji, C. M., Lawford, B. B., Maev, R. G., & Paille, J. M. (2004). "Spot weld analysis with 2D ultrasonic Arrays". Journal of Research of the National Institute of Standards and Technology, 109(2), 233. doi:10.6028/jres.109.015

[26] Cheitov, A. M., Maev, R. G., & Severin, F. M. (2007). "Acoustic Microscopy of Internal Structure of Resistance Spot Welds". IEEE Transactions on Ultrasonics, Ferroelectrics and Frequency Control, 54(8), 1521–1529. doi:10.1109/tuffc.2007.422

[27] Scott, R., Stocco, D., Chertov, A. (2022). "Using deep learning to characterize ultrasonic B-scans. ASNT 30th Research Symposium Conference Proceedings". doi.org/10.32548/rs.2022.002

APPENDICES

Appendix A

A1: Matlab Focusing Code, Phased Array Code, and Data Acquisition Code

```matlab
%----------CalculateFocalLawsWeld------FocusingCode-------------------
Can be found in [7]

%-------------AOS File Writer-------Phased Array Programmer------------

Can be found in [7] and modified for the AOS phased array system
%--------Code to Start Data Acquisition Code via Welding Pedal---------
%close all previous communication to avoid errors
% close all;
% clear all;

instrfind();
%make object with serial port
s = serial("COM5",'BaudRate', 9600);
%open up object to allow reading of data
fopen(s);
%run until AOS acquires data
while 1
    b = s.BytesAvailable; %to prevent timing out connection warning
    if b>0
        data = fgetl(s);
        number = str2num(data);
        if number >= 2.9 %Volts
%if 2.9V is found from pedal trigger(from Arduino board), then tell AOS
%to start scanning
            tic
            pause(2.5/10); %delay factor to make weld centered in scan
            % Enable pulser %
            EnableCall = mxEnableShot(deviceId,1);
            if EnableCall
                disp('Pulser enabled')
            end

            % First call for initialization %
            disp('Init acquisition (one time only)')
            [AscanCount,fifoAscanLost1,total] =
mxGetAcquisitionAscanFifoStatus(deviceId);
            while AscanCount<CycleCount;
                [AscanCount,fifoAscanLost,total] =
mxGetAcquisitionAscanFifoStatus(deviceId);
            end
            [FifoIndex,Cycle,Sequence,xPointCount,ByteSize,Signed] =
mxGetAcquisitionAscanFifoIndex(deviceId,linspace(0,CycleCount-
1,CycleCount));
            PointCount = max(xPointCount);
            Ascan = zeros(PointCount,CycleCount); %storage of all ascan

            % Loop to get the data %
            disp('Acquisition')
```

```matlab
            row = 0;
            col = 0;
            while (row~=PointCount) || (col~=CycleCount)
                [AscanCount,fifoAscanLost1,total] =
mxGetAcquisitionAscanFifoStatus(deviceId) ;

                % Cumulate Ascans %
                FifoIndex = mxGetAcquisitionAscanLifoIndex(deviceId,
linspace(0,CycleCount-1,CycleCount));
                [Ascan,Cycle,Sequence,encRawVal,lEncoder] =
mxGetAcquisitionAscanFifoData(deviceId, FifoIndex);
                [row,col] = size(Ascan);
            end

            % Get Ascan lost number %
            NascanLost = mxGetLostCountAscan(deviceId);

            % Disable pulser %
            EnableCall = mxEnableShot(deviceId,0);
            if EnableCall
                disp('Pulser disabled')
            end
            toc
            break   %exit this loop to complete program
        end
    end
end
fprintf("AOS should have acquired data.\n");
instrfind();
fclose(ans);
```

A2: Python Feature Line Detection and Filtering Code

```python
#------------------Feature Detection and Filtering Algorithm-----------
from numpy import genfromtxt
from PIL import Image
import numpy as np
import matplotlib.pyplot as plt
from scipy import ndimage
import copy
import cv2
import os


plate_one = 1.6  # insert plate 1 thickness here in (mm) (0.7 or 1.6)
(This is the plate that is closest to the transducer)
plate_two = 1.6  # insert plate 2 thickness here in (mm) (0.7 or 1.6)

if plate_one == 1.6:
    plate_one_units = 55  # The number of units here translates to the
thickness of the plate corresponding to the image
else:
    plate_one_units = 24
if plate_two == 1.6:
    plate_two_units = 55
else:
    plate_two_units = 24



def front_plate(my_data_local):
    my_data_local = my_data_local[0:150, :]
    y_max = [[my_data_local.max(axis=0)], np.argmax(my_data_local,
axis=0)]
    return my_data_local, y_max



def liquid_line_bot_left(my_data_local, full_data_local):

    my_data_local = np.flipud(np.fliplr(my_data_local[35 +
plate_one_units:110+plate_one_units + plate_two_units, 90:145]))
#Parameters for bottom left window. Orienting the image so liquid line
#is downwards
    kernel_local = np.array([[1, 0, -1],
                             [0, 1, 0],
                             [-1, 0, 1]])
    my_data_local = ndimage.convolve(my_data_local, kernel_local)
# Filtering the window to enhance negative sloped lines
    x_row_initial = my_data_local[0, 0]
    x_row = 0
    y_row = 0
    for x in range(20):
        for y in range(20):  # Searching for the peak value within this
#window which indicates the liquid line
            if x_row_initial < my_data_local[x, y]:
                x_row_initial = my_data_local[x, y]
                x_row = x
                y_row = y
    lt_1, lt_2 = traverse_downright(my_data_local, x_row, y_row)
```

```python
    lt_1 = np.flipud(lt_1)   # Reorienting the result back to its
#original form
    lt_2 = np.flipud(lt_2)
    lt_1 = [110+plate_one_units + plate_two_units-x for x in lt_1]
#Correctional line to display on M-scan in correct position
    lt_2 = [110+plate_one_units + plate_two_units-x for x in lt_2]
    for x in range(90):   # Inserting blank entries to create same
#length as M-scan
        lt_1.insert(0, float('nan'))
        lt_2.insert(0, float('nan'))
    return lt_1, lt_2


def liquid_line_bot_right(my_data_local, full_data_local):
    my_data_local = np.flipud(my_data_local[90:220, 145:200])
    kernel_local = np.array([[1, 0, -1],
                             [0, 1, 0],
                             [-1, 0, 1]])
    my_data_local = ndimage.convolve(my_data_local, kernel_local)
    x_row_initial = my_data_local[0, 0]
    x_row = 0
    y_row = 0
    for x in range(20):
        for y in range(20):
            if x_row_initial < my_data_local[x, y]:
                x_row_initial = my_data_local[x, y]
                x_row = x
                y_row = y
    lt_1, lt_2 = traverse_downright(my_data_local, x_row, y_row)
    lt_1 = [110+plate_one_units+plate_two_units-x for x in lt_1]
    lt_2 = [110+plate_one_units+plate_two_units-x for x in lt_2]
    for x in range(125+y_row):
        lt_1.insert(0, float('nan'))
        lt_2.insert(0, float('nan'))
    return lt_1, lt_2


def liquid_line_top_right(my_data_local, full_data_local):
    my_data_local = \
my_data_local[35+plate_one_units:110+plate_one_units+plate_two_units,
145:200]
    kernel_local = np.array([[1, 0, -1],
                             [0, 1, 0],
                             [-1, 0, 1]])
    my_data_local = ndimage.convolve(my_data_local, kernel_local)
    x_row_initial = my_data_local[0, 0]
    x_row = 0
    y_row = 0
    for x in range(20):
        for y in range(20):
            if x_row_initial < my_data_local[x, y]:
                x_row_initial = my_data_local[x, y]
                x_row = x
                y_row = y
    lt_1, lt_2 = traverse_downright(my_data_local, x_row, y_row)
    lt_1 = [x+35+plate_one_units for x in lt_1]
    lt_2 = [x+35+plate_one_units for x in lt_2]
```

```python
        for x in range(145+y_row):
            lt_1.insert(0, float('nan'))
            lt_2.insert(0, float('nan'))
        return lt_1, lt_2


def liquid_line_top_left(my_data_local, full_data_local):
    my_data_local = np.fliplr(my_data_local[35 +
plate_one_units:110+plate_one_units + plate_two_units, 90:145])
    kernel_local = np.array([[1, 0, -1],
                             [0, 1, 0],
                             [-1, 0, 1]])
    my_data_local = ndimage.convolve(my_data_local, kernel_local)
    x_row_initial = my_data_local[0, 0]
    x_row = 0
    y_row = 0
    for x in range(20):
        for y in range(20):
            if x_row_initial < my_data_local[x, y]:
                x_row_initial = my_data_local[x, y]
                x_row = x
                y_row = y
    lt_1, lt_2 = traverse_downright(my_data_local, x_row, y_row)
    lt_1 = np.flipud(lt_1)
    lt_2 = np.flipud(lt_2)
    lt_1 = [x+35+plate_one_units for x in lt_1]
    lt_2 = [x+35+plate_one_units for x in lt_2]
    for x in range(90-y_row):
        lt_1.insert(0, float('nan'))
        lt_2.insert(0, float('nan'))
    return lt_1, lt_2


def plate_separation(my_data_local):
    my_data_local = my_data_local[70 + plate_one_units: 140 +
plate_one_units + plate_two_units, :]  # front wall is set to be 70
#units away while one plate thickness for 1.6mm = 55units
    x_row_initial = my_data_local[0, 0]
    x_row = 0
    y_row = 0
    for x in range(5):  # To find the highest value starting position
#of cropped image within a range of rows
        for y in range(1):
            if x_row_initial < my_data_local[x, y]:
                x_row_initial = my_data_local[x, y]
                x_row = x
                y_row = y
    lt_1, lt_2 = traverse_downright(my_data_local, x_row, y_row)
    lt_1 = [x + 70+plate_one_units for x in lt_1]  # Line to align
#plate separation line with image
    lt_2 = [x + 70+plate_one_units for x in lt_2]
    return lt_1, lt_2


def traverse_downright(my_data_local, x_row, y_value):  # Function to
#detect downward sloped lines. Note: Order matters!
    line_tracker = []  # Tracks 1 values
```

```python
    line_tracker_2 = []  # Tracks 0 values. Used in case of any
#disconnections (jumps) in the tracking of lines.
    downward_diagonal = True  # Prioritizes downward sloped lines when
#true
    c = 0
    for x in range(x_row, len(my_data_local)):  # starting row to the
#last row of 125
        for y in range(y_value, len(my_data_local[0])):  # starting
#column to the last column of 255 values
            # The following if statements are used to trace lines with
#the desired value. Priority placed in negative slope direction.
            if y + c < len(my_data_local[0])-1 and x <
len(my_data_local):
                if downward_diagonal and x + 3 < my_data_local.shape[0]
and y+c+1 < my_data_local.shape[1] and my_data_local[x + 3, y + c + 1]
> 0:
                    line_tracker.append(x + 3)
                    line_tracker_2.append(float('nan'))
                    x = x + 3
                elif downward_diagonal and x + 4 <
my_data_local.shape[0] and y+c+1 < my_data_local.shape[1] and
my_data_local[x + 4, y + c + 1] > 0:
                    line_tracker.append(x + 4)
                    line_tracker_2.append(float('nan'))
                    x = x + 4
                elif x + 2 < my_data_local.shape[0] and y+c+1 <
my_data_local.shape[1] and my_data_local[x + 2, y + c + 1] > 0 and
downward_diagonal:
                    line_tracker.append(x + 2)
                    line_tracker_2.append(float('nan'))
                    x = x + 2
                elif x + 1 < my_data_local.shape[0] and y+c+1 <
my_data_local.shape[1] and my_data_local[x + 1, y + c + 1] > 0 and
downward_diagonal:
                    line_tracker.append(x + 1)
                    line_tracker_2.append(float('nan'))
                    x = x + 1
                elif x + 1 < my_data_local.shape[0] and y+c+2 <
my_data_local.shape[1] and my_data_local[x + 1, y + c + 2] > 1 and
downward_diagonal:
                    line_tracker.append(x + 1)
                    line_tracker.append(x + 1)
                    line_tracker_2.append(float('nan'))
                    line_tracker_2.append(float('nan'))
                    x = x + 1
                    c = c + 1
                elif x + 2 < my_data_local.shape[0] and y+c+2 <
my_data_local.shape[1] and my_data_local[x + 2, y + c + 2] > 1 and
downward_diagonal:
                    line_tracker.append(x + 2)
                    line_tracker.append(x + 2)
                    line_tracker_2.append(float('nan'))
                    line_tracker_2.append(float('nan'))
                    x = x + 2
                    c = c + 1
                elif x + 3 < my_data_local.shape[0] and y+c+2 <
my_data_local.shape[1] and my_data_local[x + 3, y + c + 2] > 1 and
```

```python
downward_diagonal:
                    line_tracker.append(x + 3)
                    line_tracker.append(x + 3)
                    line_tracker_2.append(float('nan'))
                    line_tracker_2.append(float('nan'))
                    x = x + 3
                    c = c + 1
                elif x + 4 < my_data_local.shape[0] and y+c+2 <
my_data_local.shape[1] and my_data_local[x + 4, y + c + 2] > 1 and
downward_diagonal:
                    line_tracker.append(x + 4)
                    line_tracker.append(x + 4)
                    line_tracker_2.append(float('nan'))
                    line_tracker_2.append(float('nan'))
                    x = x + 4
                    c = c + 1
                elif x < my_data_local.shape[0] and y+c+1 <
my_data_local.shape[1] and my_data_local[x, y + c + 1] > 0:  # position
#to the right
                    downward_diagonal = True
                    line_tracker.append(x)
                    line_tracker_2.append(float('nan'))
                elif x-1 > 0 and y+c+1 < my_data_local.shape[1] and
my_data_local[x - 1, y + c + 1] > 0:
                    line_tracker.append(x - 1)
                    line_tracker_2.append(float('nan'))
                    x = x - 1
                elif x-2 > 0 and y+c+1 < my_data_local.shape[1] and
my_data_local[x - 2, y + c + 1] > 0:
                    line_tracker.append(x - 2)
                    line_tracker_2.append(float('nan'))
                    x = x - 2
                elif x-3 > 0 and y+c+1 < my_data_local.shape[1] and
my_data_local[x - 3, y + c + 1] > 0:
                    downward_diagonal = False
                    line_tracker.append(x - 3)
                    line_tracker_2.append(float('nan'))
                    x = x - 3
                elif x-4 > 0 and y+c+1 < my_data_local.shape[1] and
my_data_local[x - 4, y + c + 1] > 0:
                    downward_diagonal = False
                    line_tracker.append(x - 4)
                    line_tracker_2.append(float('nan'))
                    x = x - 4
                elif x-5 > 0 and y+c+1 < my_data_local.shape[1] and
my_data_local[x - 5, y + c + 1] > 0:
                    downward_diagonal = False
                    line_tracker.append(x - 5)
                    line_tracker_2.append(float('nan'))
                    x = x - 5
                elif x+1 < my_data_local.shape[0] and y+c+1 <
my_data_local.shape[1] and my_data_local[x + 1, y + c + 1] == 0 and
downward_diagonal:
                    line_tracker_2.append(x + 1)
                    line_tracker.append(float('nan'))
                    x = x + 1
                elif x+2 < my_data_local.shape[0] and y+c+1 <
```

```python
my_data_local.shape[1] and my_data_local[x + 2, y + c + 1] == 0 and
downward_diagonal:
                        line_tracker_2.append(x + 2)
                        line_tracker.append(float('nan'))
                        x = x + 2
                    elif x < my_data_local.shape[0] and y+c+1 <
my_data_local.shape[1] and my_data_local[x, y + c + 1] == 0:   #
#position to the right
                        downward_diagonal = True
                        line_tracker_2.append(x)
                        line_tracker.append(float('nan'))
                    elif x-1 > 0 and y+c+1 < my_data_local.shape[1] and
my_data_local[x - 1, y + c + 1] == 0:
                        line_tracker_2.append(x - 1)
                        line_tracker.append(float('nan'))
                        x = x - 1
                    elif x-2 > 0 and y+c+1 < my_data_local.shape[1] and
my_data_local[x - 2, y + c + 1] == 0:
                        line_tracker_2.append(x - 2)
                        line_tracker.append(float('nan'))
                        x = x - 2
                    else:
                        break
            break
    # --Visual plot of lines made--
    # plt.axis([0, 255, 150, 0])
    # plt.plot(line_tracker_2, 'red')
    # plt.plot(line_tracker, 'green')
    # plt.show()
    # fig, ax = plt.subplots()
    # ax.imshow(my_data, extent=[0, 255, 125, 0])
    # ax.plot(line_tracker, 'red')
    # ax.plot(line_tracker_2, 'w')
    # plt.show()
    return line_tracker, line_tracker_2


def back_plate(my_data_local):
    my_data_local = my_data_local[70 +
plate_one_units+plate_two_units:, :]
    x_row_initial = my_data_local[0, 0]
    x_row = 0
    y_row = 0
    for x in range(5):
        for y in range(1):
            if x_row_initial < my_data_local[x, y]:
                x_row_initial = my_data_local[x, y]
                x_row = x
                y_row = y
    lt_1, lt_2 = traverse_downright(my_data_local, x_row, y_row)
    lt_1 = [x + 180 for x in lt_1]
    lt_2 = [x + 180 for x in lt_2]
    return lt_1, lt_2


def best_fit(x, y):  # Function used to detemine the function of the
    #line of best fit.
```

```python
    xbar = sum(x) / len(x)
    ybar = sum(y) / len(y)
    n = len(x)  # or len(y)

    numer = sum([xi * yi for xi, yi in zip(X, Y)]) - n * xbar * ybar
    denum = sum([xi ** 2 for xi in x]) - n * xbar ** 2

    b = numer / denum
    a = ybar - b * xbar

    print('best fit line:\ny = {:.2f} + {:.2f}x'.format(a, b))

    return a, b


def slope_intercept(lltr_1_local, llbr_1_local, lltl_1_local,
llbl_1_local):  # Function used to check if liquid lines have been
#detected.
    X1 = []
    Y1 = []
    check1 = 0
    check2 = 0
    check3 = 0
    check4 = 0
    j = 0
    count = 0
    for i in lltr_1_local:
        j = j + 1
        if str(i) != 'nan':
            X1.append(j)
            Y1.append(i)
            count = count + 1
    if count >= 20:
        a1, b1 = best_fit(X1, Y1)
        if b1 >= 0.5:
            print("Top right liquid line has been detected.\n")
            check1 = 1
    else:
        print("Insufficient top right liquid line detected\n")

    X2 = []
    Y2 = []
    j = 0
    count = 0
    for i in llbr_1_local:
        j = j + 1
        if str(i) != 'nan':
            X2.append(j)
            Y2.append(i)
            count = count + 1
    if count >= 20:
        a2, b2 = best_fit(X2, Y2)
        if b2 <= -0.5:
            print("Bot right liquid line has been detected.\n")
            check2 = 1
    else:
        print("Insufficient bot right liquid line detected\n")
```

```python
X3 = []
Y3 = []
j = 0
count = 0
for i in llbl_1_local:
    j = j + 1
    if str(i) != 'nan':
        X3.append(j)
        Y3.append(i)
        count = count + 1
if count >= 20:
    a3, b3 = best_fit(X3, Y3)
    if b3 >= 0.5:
        print("Bot left liquid line has been detected.\n")
        check3 = 1
else:
    print("Insufficient bot left liquid line detected\n")

X4 = []
Y4 = []
j = 0
count = 0
for i in lltl_1_local:
    j = j + 1
    if str(i) != 'nan':
        X4.append(j)
        Y4.append(i)
        count = count + 1
if count >= 20:
    a4, b4 = best_fit(X4, Y4)
    if b4 <= -0.5:
        print("Top left liquid line has been detected.\n")
        check4 = 1
else:
    print("Insufficient top left liquid line detected\n")
x_intercept_top = 0
y_intercept_top = 0
x_intercept_bot = 0
y_intercept_bot = 0
if check1 == 1 and check4 == 1:  # y = mx + b   y = bx + a
    x_intercept_top = round((a4-a1)/(b1-b4))
    y_intercept_top = round(b1 * x_intercept_top + a1)
if check2 == 1 and check3 == 1:  # y = mx + b   y = bx + a
    x_intercept_bot = round((a3-a2)/(b2-b3))
    y_intercept_bot = round(b3 * x_intercept_top + a3)
else:
    if check2 == 1 and x_intercept_top != 0:
        x_intercept_bot = x_intercept_top
        y_intercept_bot = round(b2 * x_intercept_top + a2)
    elif check3 == 1 and x_intercept_top != 0:
        x_intercept_bot = x_intercept_top
        y_intercept_bot = round(b3 * x_intercept_top + a3)
if check1 == 1 and check4 == 0 and x_intercept_bot != 0:
    x_intercept_top = x_intercept_bot
    y_intercept_top = round(b1 * x_intercept_bot + a1)
elif check1 == 0 and check4 == 1 and x_intercept_bot != 0:
```

```python
        x_intercept_top = x_intercept_bot
        y_intercept_top = round(b4 * x_intercept_bot + a4)
    if check1+check2+check3+check4 >= 3:
        detection = 1
    else:
        detection = 0
    return x_intercept_top, y_intercept_top, x_intercept_bot,
y_intercept_bot, detection


if __name__ == '__main__':
    marker = 0
    # output results of welds
    results_file = r"Insert location of algorithm results file here"
    manual_results_file = r"Insert location of manual results file here
"
    os.chdir(r"Insert directory here")
    with open(results_file, "w") as f:
        f.write("Results\n")
    with open(manual_results_file, "w") as f:
        f.write("Results\n")

    # Set the directory path where your files are located
    dir_path = r"Insert directory where files are located here"
    # Loop through all the files in the directory
    for filename in os.listdir(dir_path):
        if filename.endswith(".csv"):  # Change the extension to match
#your file type
            my_data = genfromtxt(filename, delimiter=',')
            full_data = my_data
            peak = np.amax(my_data[450:850, 0])  # Line to find the max
#value within the range of expected weld
            peak_value = np.where(my_data[450:850, 0] ==
np.amax(my_data[450:850, 0]))
            crop_row_1 = peak_value[0] + 450 - 70  # Crop the image to
#work with the weld
            crop_row_2 = 850 + peak_value[0] - 70
            my_data = my_data[crop_row_1[0]:crop_row_2[0], :]
            my_data1 = copy.deepcopy(my_data)
            my_data2 = copy.deepcopy(my_data)
            my_data3 = copy.deepcopy(my_data)
            my_data4 = copy.deepcopy(my_data)
            # CODE FOR IMAGING START
            kernel2 = np.array([[-1, 0, 1],
                                [-2, 0, 2],
                                [-1, 0, 1]])
            # Filter used to reduce noise from horizontal lines present
            filter2 =
ndimage.convolve(my_data2[30+plate_one_units:120+plate_one_units+plate_
two_units, 85:200], kernel2)
            # Front plate, plate sep, and back plate lines to be
#detected
            ps_1, ps_2 = plate_separation(my_data2)
            bp_1, bp_2 = back_plate(my_data2)
            fp, fp_line = front_plate(my_data2)
```

```python
my_data3[30+plate_one_units:120+plate_one_units+plate_two_units,
85:200] = filter2
            # Liquid lines to be detected
            lltr_1, lltr_2 = liquid_line_top_right(my_data3, full_data)
            llbr_1, llbr_2 = liquid_line_bot_right(my_data3, full_data)
            lltl_1, lltl_2 = liquid_line_top_left(my_data3, full_data)
            llbl_1, llbl_2 = liquid_line_bot_left(my_data3, full_data)
            # Finding maximums and minimums of liquid lines to help
#with depth penetration calculations
            top_ll_x_value, top_ll_y_value, bot_ll_x_value,
bot_ll_y_value, detection = slope_intercept(lltr_1, llbr_1, lltl_1,
llbl_1)

            # Overlaying detected lines for user visual
            # fig, ax = plt.subplots()
            # ax.imshow(my_data, extent=[0, 255, 400, 0])
            # ax.plot(fp_line[1], 'red')
            # ax.plot(ps_1, 'r')
            # ax.plot(ps_2, 'w')
            # ax.plot(bp_1, 'r')
            # ax.plot(bp_2, 'r')
            # ax.plot(lltr_1, 'r')
            # ax.plot(lltr_2, 'r')
            # ax.plot(llbr_1, 'r')
            # ax.plot(llbr_2, 'r')
            # ax.plot(lltl_1, 'r')
            # ax.plot(lltl_2, 'r')
            # ax.plot(llbl_1, 'r')
            # ax.plot(llbl_2, 'r')
            # plt.show()

            # Alternate way of finding max and min liquid line values
            highest_number = 0
            highest_number_2 = 0
            for i in llbl_1:
                if i > highest_number and i != 'nan':
                    highest_number = i
            for i in llbr_1:
                if i > highest_number_2 and i != 'nan':
                    highest_number_2 = i
            if highest_number_2 > highest_number:
                print('\nLOWER liquid lines peak index = ',
llbr_1.index(highest_number_2))
                print('LOWER liquid lines peak value = ',
highest_number_2)
                if bot_ll_y_value > highest_number_2 and
bot_ll_y_value/highest_number_2 <= 1.5:
                    ll_final_value_bot = (highest_number_2 +
bot_ll_y_value)/2
                else:
                    ll_final_value_bot = highest_number_2
            else:
                print('\nLOWER liquid lines peak index = ',
llbl_1.index(highest_number))
                print('LOWER liquid lines peak value = ',
highest_number)
                if bot_ll_y_value > highest_number:
```

```python
                                ll_final_value_bot = (highest_number +
bot_ll_y_value) / 2
                    else:
                                ll_final_value_bot = highest_number
            # After this we have index in which bottom liquid line
#minimum is.
                highest_number = 1000
                highest_number_2 = 1000
                for i in lltl_1:
                    if i < highest_number:
                                highest_number = i
                for i in lltr_1:
                    if i < highest_number_2:
                                highest_number_2 = i
                if highest_number_2 < highest_number:
                                print('\nUPPER liquid lines peak index = ',
lltr_1.index(highest_number_2))
                                print('UPPER liquid lines peak value = ',
highest_number_2)
                                if top_ll_y_value < highest_number_2:
                                        ll_final_value_top = (highest_number_2 +
top_ll_y_value) / 2
                                else:
                                        ll_final_value_top = highest_number_2
                else:
                                print('\nUPPER liquid lines peak index = ',
lltl_1.index(highest_number))
                                print('UPPER liquid lines peak value = ',
highest_number)
                                if top_ll_y_value < highest_number:
                                        ll_final_value_top = (highest_number +
top_ll_y_value) / 2
                                else:
                                        ll_final_value_top = highest_number
            # After this we have both liquid line indexes at which the
#peak/minimum occur

                # front plate correction
                front_plate_high = 0
                front_plate_low = 1000
                for i in fp_line[1]:
                    if i > front_plate_high:
                                front_plate_high = i
                for i in fp_line[1]:
                    if i < front_plate_low:
                                front_plate_low = i
                front_plate_correction = abs(front_plate_low -
front_plate_high)

                # back plate correction
                back_plate_high = 0
                back_plate_low = 1000
                for i in bp_1:
                    if i > back_plate_high:
                                back_plate_high = i
                for i in bp_1:
                    if i < back_plate_low:
```

```python
                back_plate_low = i
            back_plate_correction = abs(back_plate_low -
back_plate_high)

            # now we develop correction values for top liquid line
#which is influenced by nothing but the front plate correction
            top_liquid_line_corrected = ll_final_value_top
            bot_liquid_line_corrected = ll_final_value_bot -
back_plate_correction
            # correction for plate separation which is influenced only
#by the first plate's liquid presence
            temp1 = 0
            if len(ps_1) >= 11 and str(ps_1[10]) != 'nan' and len(ps_1)
+ len(ps_2) <= 350:
                plate_sep_corrected = ps_1[10] +
(back_plate_correction/(plate_two/plate_one + 1))
                print('Sep line corrected value = ',
plate_sep_corrected)
            elif len(ps_2) >= 11 and str(ps_2[10]) != 'nan' and
len(ps_1) + len(ps_2) <= 350:
                plate_sep_corrected = ps_2[10] +
(back_plate_correction/(plate_two/plate_one + 1))
                print('Sep line corrected value = ',
plate_sep_corrected)
            elif len(ps_1) >= 11 and len(ps_2) >= 11:
                print('\nPlate separation too prevalent throughout
weld')
                plate_sep_corrected = top_liquid_line_corrected
            else:
                print('\nPlate separation not detected')
                temp1 = 1
            # CODE FOR IMAGING END

            print("plate separation correction =", plate_sep_corrected)
            print("back plate correction =", back_plate_correction)
            print("front plate correction =", front_plate_correction)
            k = 0
            # Penetration depth of weld
            if temp1 != 1:
                pen_top_plate_mm = (plate_sep_corrected -
top_liquid_line_corrected)/(plate_sep_corrected - fp_line[1][10]) * 100
                if pen_top_plate_mm > 0 and pen_top_plate_mm <= 100:
                    print('\nPercentage Penetration front plate = ',
pen_top_plate_mm)
                else:
                    print('\nNo penetration into front plate')
                    k = 1
                pen_bot_plate_mm = (bot_liquid_line_corrected -
plate_sep_corrected)/(back_plate_high - back_plate_correction -
plate_sep_corrected) * 100
                if pen_bot_plate_mm > 0 and k == 0 and pen_bot_plate_mm
<= 100:
                    print('Percentage Penetration back plate = ',
pen_bot_plate_mm)
                else:
                    print('No penetration into back plate')
                if pen_bot_plate_mm > 0 and pen_top_plate_mm > 0 and
```

```python
pen_top_plate_mm <= 100 and pen_bot_plate_mm <= 100:
                        print('Weld detected')
                        with open(results_file, "a") as f:
                            f.write(f"{filename}: 1\n")
                    else:
                        if detection == 1:
                            print('Enough liquid lines detected to say weld
exists')
                            with open(results_file, "a") as f:
                                f.write(f"{filename}: 1\n")
                        else:
                            print('No weld detected')
                            with open(results_file, "a") as f:
                                f.write(f"{filename}: 0\n")
            # Line of code to input whether a weld has been found or
#not with 1's or 0's.
                else:
                    if detection == 1:
                        with open(results_file, "a") as f:
                            f.write(f"{filename}: 1\n")
                    else:
                        with open(results_file, "a") as f:
                            f.write(f"{filename}: 0\n")
```

A3: Python Nugget Measurement Code

```python
#---------Code Used to Measure the nugget diameter using results------
#--file created from Python feature line detection and filtering code--
# Open the text file
import re
import os
import csv
os.chdir(r"Directory goes here")

with open('results file here', 'r') as f:
    lines = f.readlines()

# Create a dictionary to store the weld groups
weld_groups = {}

# Loop through each line of the file
for line in lines:
    # Split the line into the weld number and the positions
    parts = line.strip().split(':')
    weld_num = parts[0].split('_')[0]
    position = int(parts[1].strip())

    # Add the position to the correct weld group
    if weld_num not in weld_groups:
        weld_groups[weld_num] = []
    weld_groups[weld_num].append(position)

# Create a CSV file to write the results
with open('results.csv', mode='w', newline='') as csv_file:
    fieldnames = ['Weld number', 'Result']
    writer = csv.DictWriter(csv_file, fieldnames=fieldnames)

    writer.writeheader()

    # Loop through each weld group and count the number of adjacent 1's
    for weld_num, positions in weld_groups.items():
        num_adjacent_ones = 0
        max_num_adjacent_ones = 0

        # Loop through each position in the weld group
        for position in positions:
            if position == 1:
                num_adjacent_ones += 1
                if num_adjacent_ones > max_num_adjacent_ones:
                    max_num_adjacent_ones = num_adjacent_ones
            else:
                num_adjacent_ones = 0

        # Determine the weld size based on the number of adjacent ones
        if max_num_adjacent_ones == 1:
            weld_size = 0      # "0-1.66mm"
        elif max_num_adjacent_ones == 2:
            weld_size = 0.83    # "0.83-2.49mm"
        elif max_num_adjacent_ones == 3:
            weld_size = 1.66    # "1.66-3.33mm"
        elif max_num_adjacent_ones == 4:
```

```python
        weld_size = 2.49     # "2.49-4.16mm"
    elif max_num_adjacent_ones == 5:
        weld_size = 3.33     # "3.33-4.99mm"
    elif max_num_adjacent_ones == 6:
        weld_size = 4.16     # "at least 4.16mm"
    elif max_num_adjacent_ones == 0:
        weld_size = "inconclusive"
    else:
        weld_size = 5.00   # "at least 5mm"

    # Write the weld number and weld size to the CSV file
    writer.writerow({'Weld number': weld_num, 'Result': weld_size})
```

Appendix B – Raw Data for Spot Weld Measurements

Weld Number #	Phased array (mm)	Peel Test (mm)	SAM (mm)	Cross section (mm)
0.7 + 0.7 mm Plates				
Small welds for flat, spherical, cylindrical cap geometries respectively				
1	0.83	2.50		
2	0.83	2.00		
3	0.00	1.60		
4	1.66	2.95		
5	0.83	2.55		
6	1.66	3.32		
7	0.83	2.15		
8	0.83		2.64	2.6326
9	0.00	1.70		
10	2.49	3.18	3.35	
11	1.66	3.11		
12	0.83	1.91		
13	1.66	2.83		
14	1.66		2.89	3.0407
15	2.49	3.00		
16	2.49	3.37	3.41	
17	1.66	3.05		
18	2.49	3.43		
19	0.00	1.63		
20	0.00	0.83		
21	1.66	3.32		
22	1.66		3.48	3.3770
23	0.00	1.78		
24	1.66	3.35		
25	1.66	3.55		
26	1.66	3.55		
27	1.66	3.44	3.87	
28	1.66	3.46		
29	1.66	3.42		
30	1.66	3.34		

Weld Number #	Phased array (mm)	Peel Test (mm)	SAM (mm)	Cross section (mm)
	0.7 + 0.7 mm Plates			
	Medium welds for flat, sph, cyl respectively			
1	2.49	4.26		
2	2.49	3.82		
3	2.49	4.80		
4	2.49	3.81		
5	2.49	4.50		
6	2.49	3.85		
7	2.49	3.65		
8	1.66	3.64	3.90	
9	2.49	3.90		
10	1.66		4.10	3.1434
11	2.49	4.00		
12	2.49		4.85	3.8690
13	2.49	4.47		
14	2.49	4.04	4.38	
15	2.49	3.61		
16	2.49	4.00		
17	2.49	3.69		
18	2.49	3.77		
19	2.49	3.70		
20	2.49	3.89		
21	2.49	4.71		
22	1.66		4.78	4.3036
23	2.49	4.99		
24	0.00	4.33		
25	0.83	4.20		
26	1.66	4.32		
27	2.49	4.54		
28	1.66	4.49	4.91	
29	1.66	4.40		
30	1.66	4.42		

Weld Number #	Phased array (mm)	Peel Test (mm)	SAM (mm)	Cross section (mm)
0.7 + 0.7 mm Plates				
Large welds for flat, sph, cyl respectively				
1	3.33	5.65		
2	3.33	4.50		
3	3.33	4.80		
4	3.33	4.87		
5	2.49	5.00		
6	2.49		6.28	4.9437
7	3.33	5.00		
8	3.33	5.89	6.04	
9	4.15	5.20		
10	2.49	5.73		
11	1.66	3.11		
12	0.83	1.91		
13	1.66	2.83		
14	1.66		2.89	3.0407
15	2.49	3.00		
16	2.49	3.37	3.41	
17	2.49	3.05		
18	2.49	3.43		
19	0.83	1.63		
20	0.00	0.83		
21	4.16	5.01		
22	0.00	4.54		
23	0.83	4.23		
24	2.49	4.70		
25	0.83	4.75		
26	0.00	2.22		
27	0.00	1.75		
28	0.00	2.53		
29	3.33	4.70	4.80	
30	4.16		5.90	4.8338

0.7 + 1.6 mm Plates				
Small welds for flat, sph, cyl respectively				
Weld Number #	Phased array (mm)	Peel Test (mm)	SAM (mm)	Cross section (mm)
1	1.66	3.00		
2	0.83	3.13		
3	0.83	2.50		
4	0.83	1.96		
5	1.66	2.65		
6	2.49	2.85		
7	1.66	2.95		
8	1.66		3.62	3.7446
9	2.49	3.10		
10	1.66	3.18	3.24	
11	2.49	4.96		
12	2.49	3.87		
13	2.49		4.56	3.2578
14	2.49	3.31		
15	1.66	3.51		
16	1.66	3.54		
17	2.49	3.70	4.23	
18	1.66	3.92		
19	2.49	4.10		
20	1.66	3.43		
21	1.66		3.15	2.1241
22	0.00	0.00	1.81	
23	0.00	0.00		
24	1.66	4.29		
25	0.00	0.00		
26	1.66	3.54		
27	1.66	4.40		
28	0.00	0.00		
29	0.00	0.00		
30	0.00	0.00		

0.7 + 1.6 mm Plates				
Medium welds for flat, sph, cyl respectively				
Weld Number #	Phased array (mm)	Peel Test (mm)	SAM (mm)	Cross section (mm)
1	2.49	4.60		
2	2.49	4.76		
3	1.66	4.40		
4	2.49	4.60		
5	3.33	4.25		
6	2.49	4.43	4.91	
7	0.83	4.20		
8	2.49		5.64	4.4774
9	2.49	4.10		
10	1.66	4.37		
11	0.00	4.16		
12	2.49		3.37	3.5324
13	0.00	2.03		
14	1.66	2.32		
15	2.49	2.28		
16	0.00	4.13		
17	0.00	0.00		
18	1.66	2.18		
19	0.00	0.00		
20	0.83	5.48	5.50	
21	3.33	4.80		
22	0.83	3.04		
23	2.49	3.97		
24	2.49	3.58		
25	2.49	3.50		
26	3.33	4.04		
27	0.00	0.00		
28	2.49	3.48		
29	2.49		4.21	4.3405
30	2.49	4.06	3.97	

0.7 + 1.6 mm Plates				
Large welds for flat, sph, cyl respectively				
Weld Number #	Phased array (mm)	Peel Test (mm)	SAM (mm)	Cross section (mm)
1	3.33	6.30		
2	3.33	6.21		
3	3.33	6.50		
4	4.16		6.23	5.6960
5	4.16	6.30		
6	4.16	6.35		
7	3.33	6.25		
8	4.16	6.46	6.70	
9	3.33	6.15		
10	2.49	6.30		
11	3.33	6.85		
12	3.33	6.56		
13	3.33	6.48	6.37	
14	2.49	6.29	6.30	
15	0.83			6.0943
16	0.00	6.20		
17	1.66	6.18		
18	2.49	6.36		
19	1.66	6.10		
20	1.66	6.18		
21	5.00	6.55		
22	5.00		6.52	5.8242
23	5.00	6.56		
24	5.00	6.58		
25	5.00	6.47		
26	5.00	6.18		
27	5.00	6.20	6.21	
28	5.00	6.19		
29	5.00	6.36		
30	5.00	6.41		

1.6 + 0.7 mm Plates				
Small welds for flat, sph, cyl respectively				
Weld Number #	Phased array (mm)	Peel Test (mm)	SAM (mm)	Cross section (mm)
1	2.49	2.36		
2	3.33	3.47		
3	2.49	3.33		
4	2.49	2.97	3.33	
5	2.49	2.97		
6	2.49	3.11		
7	0.00	0.00		
8	2.49		3.04	2.5907
9	0.83	1.21		
10	1.66	2.88		
11	0.00	1.48		
12	1.66	0.00	4.12	
13	0.00	0.00		
14	0.00	0.00		
15	0.00	0.00		
16	0.00	3.00	3.37	
17	0.00	0.00		
18	2.49	3.00	3.08	
19	0.00	0.00		
20	0.00	0.00		
21	1.66	2.75		
22	1.66	3.09	3.83	
23	0.00	0.00		
24	0.00	0.00		
25	0.00	0.00		
26	4.16	4.91		
27	3.33		3.38	2.3438
28	3.33	4.30		
29	2.49	2.91		
30	3.33	3.36		

1.6 + 0.7 mm Plates				
Medium welds for flat, sph, cyl respectively				
Weld Number #	Phased array (mm)	Peel Test (mm)	SAM (mm)	Cross section (mm)
1	3.33	3.97		
2	3.33		4.23	4.0031
3	4.16	4.18		
4	0.83	2.14		
5	3.33	4.19		
6	4.16	4.15		
7	2.49	3.93		
8	3.33	4.44	5.48	
9	3.33	3.73		
10	4.16	4.30		
11	2.49	5.21		
12	3.33	5.26	5.18	
13	2.49	4.44	4.60	
14	2.49	5.17		
15	3.33	4.27		
16	3.33	4.28		
17	2.49	4.63		
18	2.49	3.42		
19	0.83	2.80		
20	2.49	4.18		
21	5.00	4.72		
22	4.16	4.46	5.02	
23	3.33	3.93		
24	4.16	4.43		
25	4.16		4.60	3.3398
26	3.33	3.68		
27	3.33	3.84		
28	2.49	2.56		
29	3.33	3.68		
30	1.66	2.02		

1.6 + 0.7 mm Plates				
Large welds for flat, sph, cyl respectively				
Weld Number #	Phased array (mm)	Peel Test (mm)	SAM (mm)	Cross section (mm)
1	4.16	5.99		
2	4.16		6.32	3.9228
3	3.33	5.32		
4	4.16	5.82		
5	4.16	6.06		
6	5.00	6.89		
7	4.16	6.61		
8	4.16	6.41		
9	4.16	6.19		
10	4.16	6.53	6.30	
11	3.33		5.46	4.2301
12	2.49	6.15	5.96	
13	3.33	5.81		
14	3.33	6.20		
15	3.33	6.47		
16	3.33	6.50		
17	3.33	6.68		
18	4.16	6.31		
19	3.33	6.08		
20	3.33	6.08		
21	4.16		6.23	3.0644
22	5.00	5.55		
23	5.00	6.23		
24	4.16	4.30		
25	4.16	6.06		
26	4.16	5.14		
27	4.16	5.08		
28	0.00	1.70		
29	3.33	4.78	5.80	
30	4.16	4.83		

1.6 + 1.6 mm Plates				
Small welds for flat, sph, cyl respectively				
Weld Number #	Phased array (mm)	Peel Test (mm)	SAM (mm)	Cross section (mm)
1	0.83	2.20		
2	0.00	1.92		
3	0.00	1.95		
4	1.66		3.39	3.4232
5	0.00	0.95		
6	1.66	3.12		
7	0.83	2.80		
8	0.83	2.78		
9	0.00	1.75		
10	0.00	1.31	2.51	
11	1.66	3.50		
12	1.66	4.00		
13	1.66	3.86		
14	1.66	3.91		
15	1.66	3.94		
16	2.49		3.74	3.7758
17	1.66	2.26		
18	1.66	3.80	4.05	
19	1.66	3.10		
20	1.66	3.43		
21	2.49	2.94		
22	0.83	2.52		
23	1.66	2.35		
24	0.00	0.00		
25	1.66	2.90		
26	0.00	1.35		
27	2.49	4.10		
28	2.49	2.38		
29	0.00		4.62	4.2115
30	0.00	0.00		

1.6 + 1.6 mm Plates				
Medium welds for flat, sph, cyl respectively				
Weld Number #	Phased array (mm)	Peel Test (mm)	SAM (mm)	Cross section (mm)
1	2.49	4.00		
2	1.66			2.2231
3	2.49	4.50		
4	2.49	4.49	5.04	
5	1.66	4.62		
6	1.66	3.94		
7	1.66	4.50		
8	1.66		4.38	4.4500
9	1.66	4.30		
10	2.49	4.71		
11	3.33	4.98		
12	3.33		5.18	4.543
13	0.00	4.37		
14	2.49	4.30		
15	2.49	4.35		
16	2.49	4.60	4.96	
17	2.49	4.84		
18	3.33	4.44		
19	3.33	5.14		
20	2.49	4.20		
21	0.00	4.84		
22	0.00	4.00	4.49	
23	2.49	4.33		
24	1.66	3.38		
25	1.66		4.38	3.9537
26	3.33	4.17		
27	1.66	4.30		
28	1.66	4.22		
29	2.49	4.44		
30	2.49	4.25		

1.6 + 1.6 mm Plates				
Large welds for flat, sph, cyl respectively				
Weld Number #	Phased array (mm)	Peel Test (mm)	SAM (mm)	Cross section (mm)
1	3.33	5.40		
2	2.49	5.88		
3	2.49	5.68		
4	2.49		5.22	5.228
5	3.33	5.80		
6	2.49	6.32		
7	4.16	5.70		
8	2.49	5.97	6.41	
9	2.49	5.75		
10	2.49	5.71		
11	3.33	6.20		
12	3.33	6.12		
13	3.33	6.19		
14	3.33	6.06		
15	3.33	5.70		
16	3.33		6.12	5.5513
17	3.33	6.71		
18	3.33	5.70		
19	4.15	6.33	6.45	
20	3.33	5.52		
21	3.33	6.20		
22	2.49	5.73	5.77	
23	3.33	6.05		
24	3.33		6.28	5.9327
25	1.66	5.08		
26	3.33	6.25	6.30	
27	5.00	5.57		
28	5.00	5.08		
29	5.00	5.89		
30	4.16	5.87		

VITA AUCTORIS

NAME: Milos Draskovic

PLACE OF BIRTH: Windsor, ON

YEAR OF BIRTH: 1996

EDUCATION: Riverside Secondary School, Windsor, ON, 2014

                             University of Windsor, B.Sc., Windsor, ON, 2018

                             University of Windsor, M.Sc., Windsor, ON, 2023